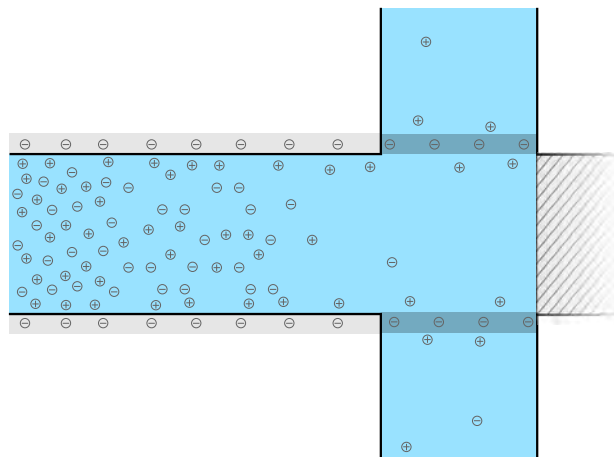


Bachelor Thesis

Electrokinetics in Microchannels with Ion-selective Membranes

Nicklas Walldorf
s103085



Supervisor: Henrik Bruus

Department of Physics
Technical University of Denmark

24 January 2014

Abstract

The aim of this bachelor's thesis is a study of electrokinetics in microchannels with ion-selective membranes. We present governing equations in electrokinetics and explain the important phenomena of a Debye screening layer formed in an electrolyte near a charged surface. Then, with applications for desalination in mind, we study an analytical and numerical model of a microchannel with an ion-selective membrane exhibiting concentration polarization (ionic depletion in front of the membrane) in an electrolyte when an electric field is applied. In particular, we study how Debye screening gives rise to overlimiting current and thus an extended depletion region. After having achieved a physical understanding of the system, we present a desalination device consisting of a cation-selective membrane and a glass 'frit' in which numerous microchannels are effectively formed. For a study of how electrokinetic effects contribute to desalination on the microscale view, we implement an outlet channel and a *leaky* wall in the numerical model. The leaky wall provides a way of modelling the porous structure of the glass frit.

Our study shows that electro-osmotic flow carries electrolyte of high ionic concentration near charged walls towards the depleted region, thus yielding a transverse concentration gradient in addition to the longitudinal concentration polarization. By studying a system with asymmetrically charged walls, we find that the transverse concentration gradient provides a considerable contribution to the concentration of the extracted electrolyte.

Furthermore, we find that charged walls do not contribute to extended depletion in the first model suggested. The extend of the depletion is determined by a vortex formed in front of the outlet channel due to the electro-osmotic flow. By applying a large transverse pressure-driven flow, we can suppress the vortex, and thus exploit overlimiting current to provide extended depletion.

Front page illustration: Sketch of a microchannel with an ion-selective membrane exhibiting concentration polarization in response to an electric field.

Resumé

Dette bachelorprojekt har til formål at studere elektrokinetik i mikrokanaler med ionselektive membraner. Indledningsvis præsenteres styrende ligninger indenfor elektrokinetikken, og det vigtige fænomen Debye afskærmning i en elektrolyt nær en ladet væg forklares. Dernæst studeres en analytisk og numerisk model af en mikrokanal med en ionselektiv membran, der udviser koncentrationspolarisation (lavkoncentrationsregion foran membranen) i en elektrolyt under påvirkning af et elektrisk felt. Specielt undersøger vi, hvordan Debye afskærmning giver anledning til 'overbegrænset' ion-transport og derved en udvidet lavkoncentrationsregion. Efter at have opnået en fysisk forståelse af systemet præsenterer vi et afsaltningsapparat bestående af en kation-selektiv membran og en glas 'frit', hvori mange mikrokanaler effektivt formes. Til at undersøge hvordan elektrokinetiske effekter påvirker afsaltningen på mikroskala, implementerer vi en afløbskanal og en *utæt* væg i den numeriske model. Den utætte væg er en måde at modellere den porøse struktur af glas fritten.

Undersøgelsen viser, at elektroosmotisk flow bærer elektrolyt af høj koncentration nær ladede vægge mod lavkoncentrationsregionen og derved bidrager til en transvers koncentrationsgradient foruden den longitudinale koncentrationspolarisation. Ved at undersøge en mikrokanal med asymmetrisk vægladning finder vi, at den transverse koncentrationsgradient bidrager væsentligt til koncentrationen af den udvundne elektrolyt.

Endvidere finder vi, at ladede vægge ikke bidrager til en udvidet lavkoncentrationsregion i den første foreslåede model. Lavkoncentrationsregionen er domineret af en hvirvel fra det elektroosmotiske flow foran afløbskanalen. Ved at påtrykke et kraftigt transvers trykdrevet flow kan vi holde opbyggelsen af hvirvlen nede, og derved udnytte overbegrænset ion-transport til at opbygge en udvidet lavkoncentrationsregion.

Preface

This bachelor's thesis is submitted in partial fulfilment of the requirements for the Bachelor of Science in Engineering degree (Physics and Nanotechnology) at the Technical University of Denmark (DTU). The work was carried out from September 2013 till January 2014 at the Department of Physics in the theoretical microfluidics group (TMF), headed by Professor Henrik Bruus. This bachelor's thesis counts as 15 ECTS credits.

I would like to thank my supervisor Professor Henrik Bruus. First, for introducing me to the field of microfluidics, a field full of exciting physics. Second, for many rewarding meetings about the project and physics in general. I have benefited greatly from his profound understanding of physics.

I would also like to thank Ph.D. student Christoffer P. Nielsen for his help, guidance, and many invaluable physical discussions during the project. I wish him all the best with his Ph.D.

A thank you should also be directed to the group at TMF for a friendly working environment and a great knowledge sharing. I have enjoyed being part of this group throughout the project.

Nicklas Walldorf
Department of Physics
Technical University of Denmark
24 January 2014

Contents

List of figures	xii
List of tables	xiii
List of symbols	xv
1 Introduction	1
1.1 Hydrodynamics and electrokinetics	1
2 Governing equations	3
2.1 Hydrodynamics	3
2.2 Electrostatics	4
2.3 Electrokinetics	5
2.4 Non-linearity	6
3 Introduction to the finite-element method	7
3.1 Weak form modeling	7
3.2 Mesh and mesh convergence	8
4 Electrolytes near solid surfaces	9
4.1 The Debye–Hückel approximation	10
4.2 The Gouy–Chapman solution	11
4.3 Numerical set-up	13
5 Microchannel with an ion-selective membrane	15
5.1 Uncharged walls	17
5.1.1 Depletion	18
5.2 Charged walls	19
5.2.1 Extended depletion region	21
5.3 Numerical set-up	22
5.3.1 Ion current density at the membrane	23
5.3.2 Symmetry and technical aspects	24
5.4 Flow	24
5.4.1 Numerical set-up	25
5.4.2 Results	27

6	Desalination	29
6.1	Symmetric wall charge	30
6.1.1	Mesh and mesh convergence	31
6.1.2	Results	33
6.2	Modified systems	36
6.2.1	Asymmetric wall charge	36
6.2.2	Transverse pressure-driven flow	37
7	Conclusion and outlook	39
A	Appendix	41
A.1	Asymmetric wall charge	41
A.2	Transverse pressure-driven flow	42

List of Figures

3.1	Sketch of triangular mesh-elements and a piecewise linear test-function	8
4.1	Sketch of the electric potential in an electrolyte near a charged surface	9
4.2	The Gouy–Chapman solution, the Debye–Hückel approximation, and numerical calculations of the electric potential	12
4.3	Numerical set-up of an electrolyte near a charged surface	13
5.1	Sketch of an electrolyte in a microchannel with an ion-selective membrane . .	15
5.2	(a) Ionic concentration and (b) electric charge density in a channel without wall charge	18
5.3	Cation current density as function of (a) electric potential difference for varying wall charges and (b) wall charge for an electric potential difference of $V_0 = 20V_T$	20
5.4	(a) Ionic concentration, (b) electric charge density, and (b) cation current density in a channel with wall charge.	21
5.5	Numerical set-up of a microchannel with a cation-selective membrane.	22
5.6	Numerical set-up of a microchannel with a cation-selective membrane including pressure and velocity fields	26
5.7	(a) x -component of the velocity for a vertical cut line through the channel. (b) Velocity field near the membrane. (c) Color surface of ionic concentration. (d) Concentration profile for varying wall charges and electric potential differences.	28
6.1	(a) Sketch of a desalination device. (b) Sketch of the suggested model with symmetrically charged walls.	29
6.2	Numerical set-up of a desalination device with symmetrically charged walls .	30
6.3	Mesh convergence plot	32
6.4	Ionic concentration of extracted electrolyte as function of flow rate	33
6.5	(a) Velocity field and (b) concentration profile in front of the outlet channel .	34
6.6	(a) Ionic concentration profile for varying widths of the outlet channel. (b) Velocity field near the membrane for an outlet channel of width $W_{\text{outlet}} = 4 \mu\text{m}$	35
6.7	Sketch of modified systems: (a) Channel with asymmetrically charged walls. (b) Channel with a transverse flow channel	37
6.8	(a) Outlet concentration for the channel with asymmetrically charged walls. (b) Outlet concentration for the channel with a transverse pressure-driven flow	38
6.9	Concentration profile for the channel with a transverse pressure-driven flow .	38
A.1	Numerical set-up of a channel with asymmetrically charged walls	41

A.2 Numerical set-up of a channel with a transverse pressure-driven flow	43
--	----

List of Tables

5.1	Physical parameters used in calculations for a microchannel with a cation-selective membrane	17
5.2	Additional boundary conditions applied for the pressure and velocity fields . .	26
6.1	Additional boundary conditions applied to the leaky wall and outlet channel .	30
6.2	Specification of the mesh used in the numerical simulations of the channel with symmetrically charged walls.	31

List of Symbols

Symbol	Description	Unit/value
c_i	Concentration of chemical species i	m^{-3}
c_{outlet}	Total ionic concentration of extracted electrolyte	m^{-3}
$\langle c_+ + c_- \rangle$	Concentration averaged over the height in a two-dimensional domain	m^{-3}
d_{mesh}	Mesh size	m
\mathbf{D}	Electric displacement	C m^{-2}
D_i	Diffusivity of chemical species i	$\text{m}^2 \text{s}^{-1}$
\mathbf{E}	Electric field	V m^{-1}
e	The elementary charge	$1.602 \times 10^{-19} \text{ C}$
\mathbf{F}_{el}	Coulomb force	N
\mathbf{f}	Body force density	N m^{-3}
H	Height of channel	m
\mathbf{J}_i	Particle current density of chemical species i	$\text{m}^{-2} \text{s}^{-1}$
k_{B}	Boltzmann constant	$1.381 \times 10^{-23} \text{ J K}^{-1}$
L	Length of channel	m
m_i	Mass of particle i	kg
N_{A}	Avogadro constant	$6.022 \times 10^{23} \text{ mol}^{-1}$
p	Pressure	N m^{-2}
\mathbf{P}	Electric polarisation	C m^{-2}
Q	Area flow rate	$\text{m}^2 \text{s}^{-1}$
q	Charge	C
\mathbf{r}	Position vector	m
Re	Reynolds number	
R_i	Reaction rate of chemical species i	$\text{m}^{-3} \text{s}^{-1}$
T	Temperature	298.15 K
V_{T}	Thermal voltage	25.7 mV (for $Z=1$)
$\mathbf{v}(\mathbf{r}, t)$	Eulerian velocity field	m s^{-1}
v_x, v_y	Velocity components	m s^{-1}
Z_i	Integer valence number of ionic species i	
ϵ_0	Vacuum permittivity	$8.854 \times 10^{-12} \text{ F m}^{-1}$

Symbol	Description	Unit/value
ϵ	Permittivity of water	$78\epsilon_0$
ζ	Zeta-potential	V
η	Dynamic viscosity	$\text{N m}^{-2} \text{s}$
λ	Intermolecular distance	m
λ^*	Typical length scale of a fluid particle	m
λ_D	Debye length	m
μ_i	Mobility of chemical species i	$\text{m}^2 \text{s}^{-1} \text{V}^{-1}$
$\rho(\mathbf{r}, t)$	Density field	kg m^{-3}
ρ_{el}	Electric charge density	C m^{-3}
$\boldsymbol{\sigma}$	Full stress tensor	N m^{-2}
$\boldsymbol{\sigma}'$	Viscous stress tensor	N m^{-2}
σ	Surface charge per area	C m^{-2}
ϕ	Electric potential	V
∇	Nabla or gradient operator	
$\nabla \cdot$	Divergence operator	
∇^2	Laplace operator	
$\boldsymbol{\Gamma}$	Flux of field variable	
$C(g)$	Relative convergence parameter	
g	Dependent variable	
g_n	Test-function	
F	Source term	
\mathbf{n}	Normal unit vector	
Ω	Region of interest	
Ω	Computational domain	
$\partial\Omega$	Domain boundary	
\mathcal{C}	Continuous functions	
$\langle \cdot \cdot \rangle$	Inner product	
$\langle \cdot \rangle$	Averaged	

1 | Introduction

The growth of population, economic development, and the effects of climate changes cause an increasing demand for pure drinking water. Global estimates differ among studies and range from 2.8 to 6.9 billions of people living in areas with high water stress around year 2050 [1, p. 194]. Desalination of seawater is a possible supply of drinking water and is becoming more widely considered with costs as the biggest concern [1, p. 559]. This thesis is a study of electrokinetics in microchannels with ion-selective membranes that has shown great potential for desalination.

In the following, we introduce some general fluidic concepts and the field of electrokinetics.

1.1 Hydrodynamics and electrokinetics

We know about fluids from our everyday life: The water we drink, the air we breathe, and the petrol we put in the car. A fluid is a substance that deforms continuously and easily when an external force is applied. The building blocks of fluids, molecules with intermolecular distances λ of approximately 0.3 nm for liquids and 3 nm for gases, appear continuous on a sufficiently large length scale. Assuming that the fluid can be described by a noninteracting classical gas, the number of molecules in a volume $(\lambda^*)^3$ follows a Poisson distribution, hence should contain $N = 4 \times 10^4$ molecules for the relative uncertainty to be $\sqrt{N}/N = 0.5\%$. This provides a typical length of a so-called continuous fluid-particle, $\lambda^* = \lambda N^{1/3} = 10$ nm (for liquids) [2, ch. 1], [3, p. 363]. For length-scales larger than λ^* we can describe the fluid as a continuum. This is the so-called continuum hypothesis.

In the field of fluidics, physical quantities are described by fields, i.e. a value is assigned to every point in space and time. We apply the Eulerian view, describing the time-evolution of the value at fixed points in space rather than following particles as in the Lagrangian description. Fields can be scalar fields, vector fields, or tensor fields, and provide an average description of physical quantities. Thus, an appropriate way to define the scalar density field is

$$\rho(\mathbf{r}, t) \equiv \frac{1}{(\lambda^*)^3} \sum_{i \in (\lambda^*)^3} m_i, \quad (1.1)$$

where m_i is the mass of particle i in the volume $(\lambda^*)^3$ centred at \mathbf{r} . We define the vector velocity field by

$$\mathbf{v}(\mathbf{r}, t) \equiv \frac{1}{\rho(\mathbf{r}, t)(\lambda^*)^3} \sum_{i \in (\lambda^*)^3} m_i \mathbf{v}_i, \quad (1.2)$$

[2, p. 6-7].

An important class of fluids is collected under the term of electrolytes, i.e. aqueous solutions of dissolved ionic species. The forces acting on charged particles provide some important characteristics of electrolytes. The motion of electrolytes relative to charged surfaces is studied in the field of electrokinetics [2, p. 143]. Displacements of a charged particle in a fluid is governed by advection due to a velocity field of the fluid, diffusion due to random thermal motion of particles, and displacement by an electric field [4, ch. 4]. This thesis provides a study of electrokinetics in microchannels with ion-selective membranes, in particular with applications for desalination in mind.

In chapter 2, we present governing equations in the field of electrokinetics. In chapter 4, we consider the behaviour of an electrolyte near a charged surface. In particular, we explain the important phenomena of the Debye screening layer formed when counterions are attracted to a charged surface and co-ions are repelled. In chapter 5, we present and analyse a model of an electrokinetic system with an ion-selective membrane exhibiting concentration polarization in an electrolyte in response to an electric field. As we will see, this effect has great potential for desalination. In chapter 6, we present and discuss a desalination device.

Throughout the thesis, simulations are carried out using the finite-element method with the commercial software COMSOL. Both for verification of the analytical results and for further studies of the systems beyond analytical models. An introduction to the finite-element method is given in chapter 3.

2 | Governing equations

The following sections introduce the governing equations applied in the study of the electrokinetic systems presented in this thesis.

2.1 Hydrodynamics

Throughout the thesis, we apply the continuum hypothesis as discussed in the introduction. As long as we consider the system on a length scale larger than the typical size of a fluid-particle, the continuum hypothesis is a good approximation. In non-relativistic mechanics, mass in a volume Ω can change only by a mass flux through the surface $\partial\Omega$. This gives rise to the continuity equation

$$\partial_t \rho = -\nabla \cdot (\rho \mathbf{v}), \quad (2.1)$$

i.e. the rate of change in density at a point in space and time is caused by a convergence of mass-current density to that point. For an incompressible fluid where ρ is constant in space and time

$$\nabla \cdot \mathbf{v} = 0. \quad (2.2)$$

The equation of motion of the fluid is found by applying the Eulerian description and considering the change of momentum of the fluid inside a fixed volume Ω caused by convection through the surface $\partial\Omega$ and by Newton's second law. This leads to

$$\rho(\partial_t \mathbf{v} + (\mathbf{v} \cdot \nabla) \mathbf{v}) = \nabla \cdot \boldsymbol{\sigma} + \mathbf{f}, \quad (2.3)$$

where $\boldsymbol{\sigma}$ is the full stress tensor and \mathbf{f} is the total body force density. We consider electrostatic and gravitational body forces. However, the gravitational body force is cancelled by the hydrostatic pressure, hence, we do not include the gravitational force explicit in \mathbf{f} and let p denote the external pressure. Note that the term on the left side of equation (2.3) is the resulting force density where we have applied the material time derivative of the Eulerian velocity field to correct from the Eulerian description to ordinary Newtonian mechanics.

The components of the full stress tensor $\boldsymbol{\sigma}$ are

$$\sigma_{ij} = -p\delta_{ij} + \sigma'_{ij} = -p\delta_{ij} + \eta(\partial_j v_i + \partial_i v_j) + (\beta - 1)\eta(\partial_k v_k)\delta_{ij}, \quad (2.4)$$

governing the pressure p and viscosity. η is the dynamic viscosity (in units of Pa s) characterising internal friction due to shear stress, and β is the dimensionless viscosity ratio characterising the ratio of internal friction due to compression (second viscosity ζ) and dynamic viscosity. The dynamic viscosity for water has a high dependence on temperature, however at room

temperature it is around 1 mPa s. The second viscosity is only relevant for compressible fluids which is not considered in this thesis.

For constant viscosity coefficients, equation (2.3) leads to the Navier–Stokes equation

$$\rho[\partial_t \mathbf{v} + (\mathbf{v} \cdot \nabla) \mathbf{v}] = -\nabla p + \eta \nabla^2 \mathbf{v} + \beta \eta \nabla (\nabla \cdot \mathbf{v}) + \mathbf{f}, \quad (2.5)$$

$$\rho[\partial_t \mathbf{v} + (\mathbf{v} \cdot \nabla) \mathbf{v}] = -\nabla p + \eta \nabla^2 \mathbf{v} + \mathbf{f}, \quad (\text{incompressible fluid}). \quad (2.6)$$

Note that, intuitively, $\eta \nabla^2 \mathbf{v}$ arises from a difference in stress just as ∇p arises from a difference in pressure.

By introducing the dimensionless position $\tilde{\mathbf{r}} = r_0^{-1} \mathbf{r}$, velocity $\tilde{\mathbf{v}} = v_0^{-1} \mathbf{v}$, time $\tilde{t} = v_0/r_0 t$, and pressure $\tilde{p} = r_0/(\eta v_0) p$, and setting $\mathbf{f} = 0$, we write the incompressible Navier–Stokes equation (2.6) in the dimensionless form

$$Re[\partial_{\tilde{t}} \tilde{\mathbf{v}} + (\tilde{\mathbf{v}} \cdot \tilde{\nabla}) \tilde{\mathbf{v}}] = -\tilde{\nabla} \tilde{p} + \tilde{\nabla}^2 \tilde{\mathbf{v}}, \quad (2.7)$$

where

$$Re \equiv \frac{\rho v_0 r_0}{\eta} \quad (2.8)$$

is the Reynolds number that determines whether the non-linear left-hand side or the linear right-hand side dominates in the system.

[2, ch. 2, 3].

2.2 Electrostatics

We assume sufficiently low velocities of the ionic species and consider the system in the electrostatic approximation. Electrostatics couple with hydrodynamics through the body force density in the Navier–Stokes equation. Charged particles exert Coulomb forces on each other. The force on a test charge q is governed by the electric field \mathbf{E} ,

$$\mathbf{F}_{\text{el}} = q \mathbf{E}. \quad (2.9)$$

When describing electric fields in matter, we introduce the electric displacement \mathbf{D} defined by

$$\mathbf{D} \equiv \epsilon_0 \mathbf{E} + \mathbf{P} = \epsilon \mathbf{E}, \quad (2.10)$$

where $\epsilon_0 = 8.854 \times 10^{-12} \text{ F m}^{-1}$ is the vacuum permittivity, and \mathbf{P} is the polarization induced in the material, defined as dipole moments per unit volume. The last equality is valid for a linear isotropic dielectric. We consider aqueous solutions which satisfy this approximation. Thus, $\epsilon = 78\epsilon_0$ here denotes the permittivity of water and governs the polarization response of water to an electric field [2, p. 147].

According to Gauss’s law, the flux through a surface $\partial\Omega$ enclosing a free charge q_{free} is

$$\oint_{\partial\Omega} \mathbf{d}\mathbf{a} \cdot \mathbf{D} = q_{\text{free}}. \quad (2.11)$$

Since the integral of the electric field around a closed path is zero (for zero magnetic field or sufficiently small time-variation of the magnetic field), the curl is zero, and thus in the

electrostatic regime, the electric field can be fully described by the gradient of the scalar electric potential ϕ

$$\mathbf{E} = -\nabla\phi, \quad (2.12)$$

where the electric potential is defined with respect to some reference point \mathcal{O}

$$\phi = -\int_{\mathcal{O}}^r \mathbf{dl} \cdot \mathbf{E}. \quad (2.13)$$

Combining the differential form of equation (2.11) with equation (2.12), we find the useful Poisson's equation for a linear isotropic dielectric

$$\nabla^2\phi = -\frac{\rho_{\text{el}}}{\epsilon}, \quad (2.14)$$

where ρ_{el} is the electric charge density. [2, ch. 8], [5].

2.3 Electrokinetics

As discussed in the introduction, transport of a charged particle i in a fluid is governed by advection, diffusion, and displacement by an electric field. These phenomena contribute to a particle current density \mathbf{J}_i , i.e. a number of particles crossing a unit area per unit time, coupled to the particle concentration c_i by conservation of particles

$$\partial_t c_i = -\nabla \cdot \mathbf{J}_i + R_i, \quad (2.15)$$

where the rate of change in concentration at a point in space is either due to a convergence of particle current density or to some chemical reactions producing c_i with rate R_i . We give the concentration in units of M (mole per litre). Note that in aqueous solutions $1 \text{ mM} \approx N_{\text{A}} \text{ m}^{-3}$, where N_{A} is the Avogadro constant. The ionic particle current density is coupled to the electric current density $\tilde{\mathbf{J}}_i$ by $\tilde{\mathbf{J}}_i = \mathbf{J}_i |Z_i| e$, where Z_i is the valence number of the ionic species i .

The advective current density is given as the concentration of the ionic species i times the velocity of the fluid. Diffusion is governed by a concentration gradient since particles displace from high to low concentration. A linear approximation is given by Fick's law

$$\mathbf{J}_i^{\text{diff}} = -D_i \nabla c_i, \quad (2.16)$$

where D_i is the diffusivity in units of $\text{m}^2 \text{ s}^{-1}$. For typical small ions in an aqueous solution, the diffusivity is of the order of $10^{-9} \text{ m}^2 \text{ s}^{-1}$. In particular relevance for desalination, we note that the diffusivity for small concentrations of Na^+ and Cl^- in aqueous solutions at $T = 25^\circ \text{C}$ is $1.33 \times 10^{-9} \text{ m}^2 \text{ s}^{-1}$ and $2.03 \times 10^{-9} \text{ m}^2 \text{ s}^{-1}$, respectively [2, p. 145].

In the presence of an electric field, a particle of charge q initially at rest is accelerated due to the Coulomb force (2.9). When the particle gains velocity, the viscous drag force eventually balances the coulomb force and the particle reaches a steady-state velocity $\mathbf{v} = \mu \mathbf{E}$, where μ is the mobility in units of $\text{m}^2 \text{ s}^{-1} \text{ V}^{-1}$. The mobility for small concentrations of Na^+ and Cl^- in aqueous solutions at $T = 25^\circ \text{C}$ is $5.19 \times 10^{-8} \text{ m}^2 \text{ s}^{-1} \text{ V}^{-1}$ and $-7.91 \times 10^{-8} \text{ m}^2 \text{ s}^{-1} \text{ V}^{-1}$, respectively [2, p. 145]. The contribution to the particle current density is

$$\mathbf{J}_i^{\text{el}} = -c_i \mu_i \nabla \phi. \quad (2.17)$$

For small concentrations, the particle concentration follows Boltzmann statistics in thermal equilibrium, and the diffusivity and mobility is related through the Einstein relation $D_{\pm} = \pm V_T |\mu_{\pm}|$, where $V_T = k_B T / (|Z|e)$ is the thermal voltage and plus and minus denote a positively and a negatively charged particle, respectively [2, p. 242], [3, p. 210]. At room temperature for $Z = \pm 1$, $V_T = 25.7$ mV.

Adding up the contributions, we reach the Nernst–Planck equation

$$\mathbf{J}_{\pm} = c_{\pm} \mathbf{v} - D_{\pm} \nabla c_{\pm} \mp c_{\pm} D_{\pm} V_T^{-1} \nabla \phi. \quad (2.18)$$

[2, ch. 8, 9], [4, ch. 4].

2.4 Non-linearity

The Navier–Stokes equation contains the non-linear term $(\mathbf{v} \cdot \nabla) \mathbf{v}$ which makes it difficult to find analytical solutions. For the physical insight, we provide some important analytical flow solutions in section 5.4. For the numerical study presented in chapter 5, we assume sufficiently low Reynolds number and neglect this non-linear contribution. Even so, coupling between the governing equations introduce a strong non-linearity in the system. Chapter 4 provides an example of such a coupling. However in that case, an analytical solution can actually be found for the very symmetric geometry considered. In general, when considering more complex geometries, one have to apply numerical methods. The following chapter provides an introduction to the numerical finite-element method.

3 | Introduction to the finite-element method

Simulations are carried out using the finite-element method with COMSOL. In the finite-element method, the physical continuum is separated into a finite number of mesh-elements. This chapter provides a brief overview of the basic ideas behind weak form modeling in the finite-element method.

3.1 Weak form modeling

We consider inhomogeneous boundary value problems written in the form of continuity equations

$$\nabla \cdot \mathbf{\Gamma} = F, \quad (3.1)$$

where the flux $\mathbf{\Gamma}$ of the field variable $g(\mathbf{r})$ is given by a differential operator \mathcal{D} acting on g . F is the source plus rate of change of g . This form is applicable for field problems treating flows or conservation of quantities such as mass (2.1), momentum (2.3), electric field lines (2.14), or particles (2.15) and is applicable for all governing equations in this thesis.

We assume that g can be represented in a finite basis of real functions $\{g_1, g_2, \dots, g_N\}$ that nearly spans the function space

$$g(\mathbf{r}) \approx \sum_{n=1}^N G_n g_n(\mathbf{r}), \quad (3.2)$$

where the coefficients G_n are to be determined. In COMSOL, g_n are denoted test-functions and are constructed by some specific function associated with each node of the mesh, as clarified below. From equation (3.1), we define the defect d as

$$d = \nabla \cdot \mathbf{\Gamma} - F. \quad (3.3)$$

For a so-called strong solution satisfying equation (3.1), the defect is zero. We expand the defect in basis of g_n , and require the expansion coefficients to vanish for equation (3.1) to be approximately satisfied

$$\langle g_n | d \rangle = \langle g_n | \nabla \cdot \mathbf{\Gamma} - F \rangle = \int_{\Omega} d\mathbf{r} [g_n \nabla \cdot \mathbf{\Gamma} - g_n F] = 0. \quad (3.4)$$

A solution that satisfies equation (3.4) is called a weak solution. Using that $\nabla \cdot \{g_n \mathbf{\Gamma}\} = g_n \nabla \cdot \mathbf{\Gamma} + \nabla g_n \cdot \mathbf{\Gamma}$, we find by Gauss's theorem

$$\int_{\partial\Omega} da g_n \mathbf{n} \cdot \mathbf{\Gamma} + \int_{\Omega} d\mathbf{r} [-\nabla g_n \cdot \mathbf{\Gamma} - g_n F] = 0. \quad (3.5)$$

This is the weak form suitable for numerical simulations in COMSOL. By applying the expansion (3.2), this is turned into a matrix equation for G_n . Note that the governing equations in chapter 2 contain only up to second-order derivatives ($\mathbf{\Gamma}$ contain up to first-order derivatives), and g need only be continuous and piecewise differentiable for (3.5) to be well-defined [6], [2, p. 325-327].

3.2 Mesh and mesh convergence

The mesh consists of triangular mesh-elements T . The discrete set of triangles is denoted \mathcal{T} . Note that a linear function of two variables

$$p \in \mathbb{P}_1 = \{a_0 + a_1x_1 + a_2x_2 | a_0, a_1, a_2 \in \mathbb{R}\}, \quad (3.6)$$

is uniquely determined by its values on the vertices (nodes) of a non-degenerate triangle. We define the solution space of continuous piecewise linear functions of two variables

$$V = \left\{ g \in \mathcal{C}(\bar{\Omega}) \mid g|_T \in \mathbb{P}_1, \quad \forall T \in \mathcal{T} \right\}. \quad (3.7)$$

Functions in V are piecewise differentiable as needed in equation (3.5). If we denote a node in the mesh by \mathbf{p}_m , there exists a unique function such that $g_n(\mathbf{p}_m) = \delta_{mn}$. These test-functions form a finite basis for V [7]. The test-functions can also be (and typically are) of higher degree than first order polynomials.

Mesh convergence

In order for the test-functions to span the solution space properly, the mesh elements must be sufficiently small. However, a decrease in mesh element size d_{mesh} , where d_{mesh} denotes a characteristic length of the mesh elements, increases the computational time. A mesh convergence analysis is performed by comparing solutions for decreasing mesh element size. We define the relative convergence parameter $C(g)$ of the field variable $g(\mathbf{r})$ by

$$C(g) = \sqrt{\frac{\int dx dy (g - g_{\text{ref}})^2}{\int dx dy g_{\text{ref}}^2}}, \quad (3.8)$$

where the reference solution g_{ref} is the solution to the smallest d_{mesh} [8]. In COMSOL, the relative convergence parameter is found by sweeping over different values of d_{mesh} and applying the JOIN function to find the difference to the reference solution.

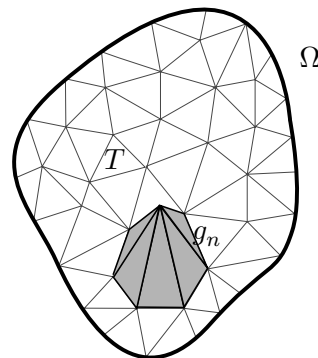


Figure 3.1: Sketch of triangular mesh-elements T in the domain Ω , and a piecewise linear test-function g_n [6].

4 | Electrolytes near solid surfaces

Near a charged surface, ions in an electrolyte form a screening layer, the so-called Debye layer. The following sections provide an explanation and an analytical model of this electrokinetic phenomena. The chapter serves as an introduction to theoretical and numerical considerations in electrokinetics, and a thorough understanding of the Debye layer is important for the study of the electrokinetic system presented in chapter 5.

When an electrolyte gets in contact with a solid surface, a charge transfer often appears. In the case of glass, Si-OH (silanol group) at the surface loses a proton in the presence of an aqueous solution and leaves negatively charged Si-O⁻ on the surface [4, ch. 1].

Consider a binary Z:Z electrolyte, i.e. an aqueous solution of anions and cations with equal concentration c_0 and equal absolute valence $|Z|$ [9], near a positively charged infinite planar surface in the xz -plane at $y = 0$, as illustrated in figure 4.1. Counterions are attracted to the oppositely charged surface and co-ions are repelled. Due to thermal behaviour of the particles, the transport is governed by statistical physics. However, since this statistical behaviour is build into the Nernst–Planck equation through Fick’s law, we find the ionic distribution by

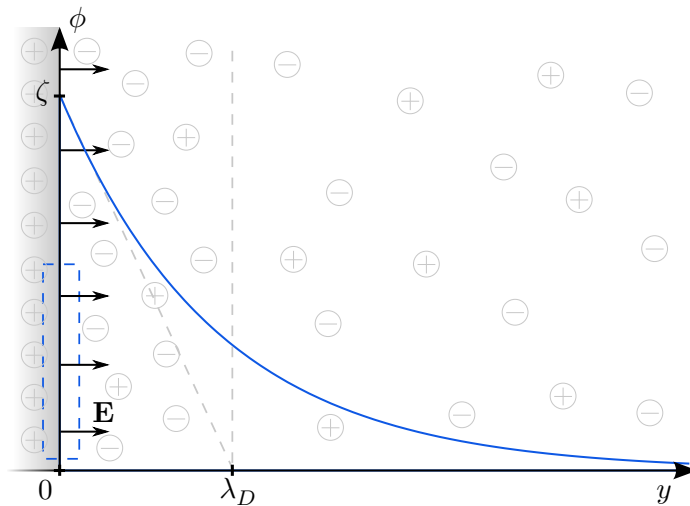


Figure 4.1: Sketch of the electric potential ϕ in a binary electrolyte as function of distance y from a positively charged surface. Anions are attracted to the surface, and cations are repelled. The Debye length λ_D is marked on the y -axis, and the corresponding Debye layer is marked with a vertical grey dashed line. Electric field lines are drawn from the charged surface together with a Gaussian pillbox, marked with a blue dotted line.

requiring the ion current densities (2.18) to vanish in equilibrium

$$\mathbf{J}_{\pm} = -D_{\pm} \nabla c_{\pm} \mp c_{\pm} D_{\pm} V_T^{-1} \nabla \phi = 0 \quad \Leftrightarrow \quad (4.1a)$$

$$\frac{\nabla c_{\pm}}{c_{\pm}} = \nabla \ln(c_{\pm}) = \mp V_T^{-1} \nabla \phi. \quad (4.1b)$$

The potential at the surface is known as the zeta-potential, $\phi(0) = \zeta$. For glass and an aqueous solution of pH 7, the zeta-potential is of the order -100 mV [4, ch. 1].

Infinitely far away from the surface, the electrolyte cannot feel the charged wall, thus, $\phi(\infty) = 0$ and $c_{\pm}(\infty) = c_0$. Applying these boundary conditions yields

$$c_{\pm}(\mathbf{r}) = c_0 \exp\left(\mp \frac{\phi(\mathbf{r})}{V_T}\right). \quad (4.2)$$

To obtain a differential equation for the electric potential, equation (4.2) is inserted into Poisson's equation (2.14)

$$\nabla^2 \phi(\mathbf{r}) = -\frac{1}{\epsilon} \rho_{\text{el}}(\mathbf{r}) = -\frac{1}{\epsilon} Ze(c_+(\mathbf{r}) - c_-(\mathbf{r})) = \frac{2Zec_0}{\epsilon} \sinh\left(\frac{\phi(\mathbf{r})}{V_T}\right). \quad (4.3)$$

This illustrates how non-linearity is introduced into the system due to coupling of the governing equations. In general, we must turn to approximations or numerical methods to solve this non-linear differential equation. However, an analytical solution can be found for the simple infinite planar surface considered here. [10, 2, 4].

4.1 The Debye–Hückel approximation

First, we consider an approximate solution to equation (4.3). For sufficiently high temperatures, $V_T \gg |\zeta|$, and we can linearise the hyperbolic sine in (4.3)

$$\nabla^2 \phi(\mathbf{r}) = \frac{1}{\lambda_D^2} \phi(\mathbf{r}), \quad (4.4)$$

where we have introduced the Debye length

$$\lambda_D \equiv \sqrt{\frac{\epsilon k_B T}{2(Ze)^2 c_0}} = \sqrt{\frac{\epsilon V_T}{2Zec_0}}. \quad (4.5)$$

For a binary 1:1 electrolyte with permittivity $\epsilon = 78\epsilon_0$ and ionic concentration $c_0 = 1$ mM (of both cations and anions), the Debye length is 9.6 nm (for $T = 25$ °C).

We have already mentioned that a typical zeta-potential is of the order -100 mV and that $V_T = 25.7$ mV at room temperature for a monovalent ionic species. Thus, the Debye–Hückel approximation is almost never satisfied. However, qualitatively, the Debye–Hückel approximation provides a great physical insight.

Note furthermore, that the Debye length is of the same order as a fluid-particle defined in the introduction. Hence, we approach the length scale where the continuum hypothesis is no longer valid. However, the model provides results in agreement with experimental observations [4, p. 199], and we therefore take this model as valid, but are aware of that we should be careful in this small length scale.

For the system considered in figure 4.1, symmetry reduces the problem to

$$\partial_y^2 \phi(y) = \frac{1}{\lambda_D^2} \phi(y). \quad (4.6)$$

By applying the boundary conditions from before, we find an expression for the electric potential

$$\phi(y) = \zeta \exp\left(-\frac{y}{\lambda_D}\right) \quad , \quad y \geq 0. \quad (4.7)$$

The Debye length provides a characteristic length of the area of increased counterion concentration, as illustrated in figure 4.1. Equation (4.5) reveals the diffusive and electric contribution to the Debye layer. The Debye length squared is proportional to the thermal voltage, hence, diffusion tends to move the screening ions further out into the bulk, and inversely proportional to a contribution from the electrostatic potential, $2Zec_0/\epsilon$ from equation (4.4), which tends to draw the screening ions closer to the surface.

The charge per area q_{liq} in the Debye layer that screens the positively charged surface is given by

$$q_{\text{liq}} = \int_0^\infty dy \rho_{\text{el}}(y) = \int_0^\infty dy \left[-\epsilon \partial_y^2 \phi(y) \right] = \int_0^\infty dy \left[\frac{-\epsilon \zeta}{\lambda_D^2} \exp\left(-\frac{y}{\lambda_D}\right) \right] = -\frac{\epsilon}{\lambda_D} \zeta. \quad (4.8)$$

The system acts as a capacitor, with capacitance per area $C_D = -q_{\text{liq}}/\zeta = \epsilon/\lambda_D$, since electric charge is accumulated due to the electric potential difference of the solid surface and the bulk [2, ch. 8]. We might regard the surface as a positive plate and the Debye layer as a negative "plate" in a parallel-plate capacitor with equal charge on the plates (the Debye layer screens the charged surface). The electric fields cancel outside the capacitor and add up inside the capacitor [5, p. 74]. Effectively, field lines run perpendicular from the charged surface to the Debye layer, as illustrated in figure 4.1. The surface charge per area σ can thus be calculated by considering a Gaussian pillbox, as illustrated in figure 4.1 with a blue dashed line. By Gauss's law we find

$$\oint_{\partial\Omega} \mathbf{da} \cdot \mathbf{E} = \mathbf{E}(0) \cdot \hat{\mathbf{y}} A = \frac{\sigma A}{\epsilon} \quad \Leftrightarrow \quad \sigma = \epsilon \mathbf{E}(0) \cdot \hat{\mathbf{y}} = -\epsilon \partial_y \phi(0) = \frac{\epsilon}{\lambda_D} \zeta. \quad (4.9)$$

We notice that $q_{\text{liq}} = -\sigma$, thus ensuring global charge neutrality.

4.2 The Gouy–Chapman solution

For the simple infinite planar surface considered here, an exact solution to equation (4.3) can be found, the so-called Gouy–Chapman solution. By introducing $y = \lambda_D \tilde{y}$, $\phi = V_T \tilde{\phi}$, we write equation (4.3) in dimensionless form

$$\frac{V_T}{\lambda_D^2} \partial_{\tilde{y}}^2 \tilde{\phi}(\tilde{y}) = \frac{2Zec_0}{\epsilon} \sinh\left(\tilde{\phi}(\tilde{y})\right) \quad \Leftrightarrow \quad \partial_{\tilde{y}}^2 \tilde{\phi}(\tilde{y}) = \sinh\left(\tilde{\phi}(\tilde{y})\right), \quad (4.10)$$

where symmetry has reduced the problem to one dimension. We multiply with $\tilde{\phi}'$, where prime denotes differentiation with respect to \tilde{y} , and find

$$\tilde{\phi}'(\tilde{y}) \tilde{\phi}''(\tilde{y}) = \tilde{\phi}'(\tilde{y}) \sinh\left(\tilde{\phi}(\tilde{y})\right) \quad \Leftrightarrow \quad \left(\frac{1}{2} [\tilde{\phi}'(\tilde{y})]^2\right)' = \left(\cosh(\tilde{\phi}(\tilde{y}))\right)'. \quad (4.11)$$

Infinitely far from the wall, we require that $\phi'(\infty) = 0$. Furthermore, since we have assumed a positively charged surface, we choose the negative sign when isolating $\tilde{\phi}'$

$$\tilde{\phi}'(\tilde{y}) = -\sqrt{2 \cosh(\tilde{\phi}(\tilde{y})) - 2} = -2 \sinh\left(\frac{1}{2}\tilde{\phi}(\tilde{y})\right). \quad (4.12)$$

Substituting $u = 1/2\tilde{\phi}$, we find by separation of variables¹

$$\tanh\left(\frac{u(\tilde{y})}{2}\right) = \tanh\left(\frac{\zeta}{4V_T}\right) \exp(-\tilde{y}), \quad (4.13)$$

satisfying $\phi(0) = \zeta$. Substituting back to physical variables, we reach the Gouy–Chapman solution for the electric potential

$$\phi(y) = 4V_T \operatorname{arctanh}\left[\tanh\left(\frac{\zeta}{4V_T}\right) \exp\left(-\frac{y}{\lambda_D}\right)\right], \quad y \geq 0. \quad (4.14)$$

For $V_T \gg |\zeta|$, $\tanh(u) \approx u$ and $\operatorname{arctanh}(u) \approx u$, hence, equation (4.14) reduces to the Debye–Hückel approximation. A numerical verification of the result is presented in the following section.

The Gouy–Chapman solution is plotted in figure 4.2 together with the Debye–Hückel approximation and numerical calculations for $V_T = 26$ mV, $Z = 1$, $\epsilon = 78\epsilon_0$, and $c_0 = 1$ mM. For $V_T \gg |\zeta|$, the Debye–Hückel approximation is close to the exact result. However, for larger absolute values of the zeta-potential, the Debye–Hückel begins to deviate from the Gouy–Chapman solution.

¹Using that $\int du \frac{1}{\sinh(u)} = \ln\left(\tanh\left(\frac{u}{2}\right)\right) + c$

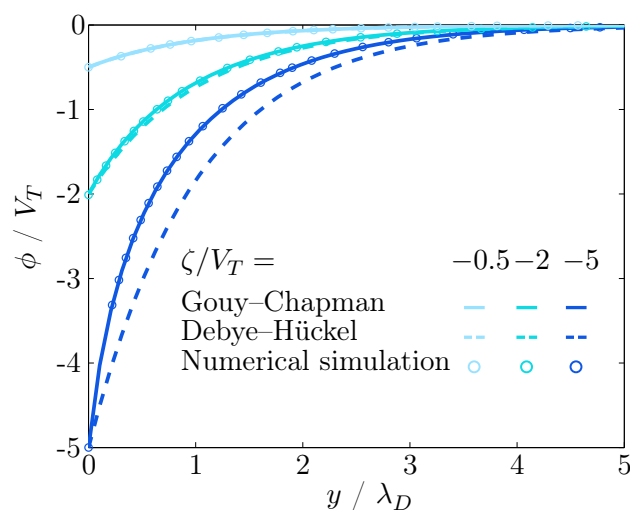


Figure 4.2: The Gouy–Chapman solution, the Debye–Hückel approximation, and numerical calculations of the electric potential in an electrolyte as function of distance y from a charged surface.

The relation between surface charge and zeta-potential for the Gouy–Chapman solution is found from equation (4.12) by applying Gauss' law

$$\sigma = \frac{2\epsilon V_T}{\lambda_D} \sinh\left(\frac{\zeta}{2V_T}\right). \quad (4.15)$$

4.3 Numerical set-up

The numerical set-up is illustrated in figure 4.3, where governing equations and boundary conditions are labelled by their equation-references on the corresponding domain Ω and boundaries $\partial\Omega_i$.

Ionic concentration

At steady-state, assuming that no chemical reactions occur, equation (2.15) becomes

$$\nabla \cdot \mathbf{J}_{\pm} = 0, \quad (4.16)$$

where the ion current densities, given by equation (2.18) for $\mathbf{v} = 0$, are functions of the dependent variables c_+ and c_- . In weak form (4.16) becomes

$$\int_{\partial\Omega} da c_{\pm,n} \mathbf{n} \cdot \mathbf{J}_{\pm} + \int_{\Omega} d\mathbf{r} [-\nabla c_{\pm,n} \cdot \mathbf{J}_{\pm}] = 0, \quad (4.17)$$

where $c_{\pm,n}$ denotes the test-functions for the ionic concentrations and \mathbf{n} denotes the normal unit vector pointing out of the domain.

No particle flux is allowed through the walls, hence, we apply the weak contribution

$$\mathbf{n} \cdot \mathbf{J}_{\pm}(\mathbf{r}) = 0, \quad (4.18)$$

for $\mathbf{r} \in \{\partial\Omega_2, \partial\Omega_3\}$.

At the inlet and outlet we apply the constraints

$$c_{\pm}(\mathbf{r}) = c_0, \quad (4.19)$$

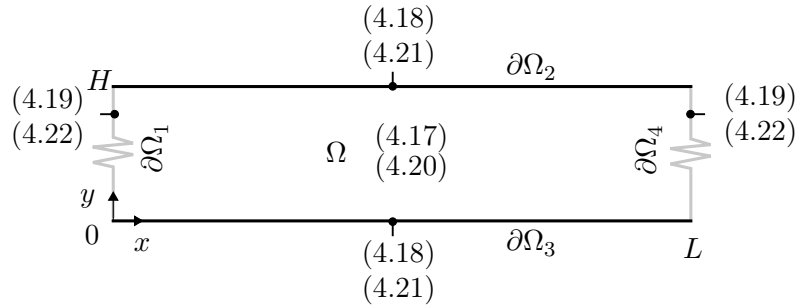


Figure 4.3: Schematic illustration of the numerical set-up of an electrolyte near a charged surface. Ω denotes the domain, H refers to the height of the domain (length of boundaries $\partial\Omega_1$ and $\partial\Omega_4$), and L refers to the length of the domain (length of $\partial\Omega_2$ and $\partial\Omega_3$). Rigid walls are black, and non-rigid boundaries are grey. Numbers in parenthesis refer to the equation number of the governing equation or boundary condition.

for $\mathbf{r} \in \{\partial\Omega_1, \partial\Omega_4\}$.

Electric potential

In weak form Poisson's equation becomes

$$\int_{\partial\Omega} da \phi_n \mathbf{n} \cdot (-\epsilon \nabla \phi) + \int_{\Omega} d\mathbf{r} [-\nabla \phi_n \cdot (-\epsilon \nabla \phi) - \phi_n \rho_{\text{el}}] = 0, \quad (4.20)$$

where $\rho_{\text{el}} = Ze(c_+ - c_-)$.

At the walls, we have in agreement with equation (4.9) the weak contribution

$$\mathbf{n} \cdot (-\epsilon \nabla \phi) = -\sigma, \quad (4.21)$$

and set $\sigma(\mathbf{r}) = 0$ for $\mathbf{r} \in \{\partial\Omega_2\}$ and apply equation (4.15) for $\mathbf{r} \in \{\partial\Omega_3\}$.

At the inlet and outlet we apply the constraint

$$\phi(\mathbf{r}) = 0, \quad (4.22)$$

for $\mathbf{r} \in \{\partial\Omega_1, \partial\Omega_4\}$.

Note that the boundary conditions near the charged wall at the inlet and outlet are unphysical and contradict the formation of a Debye layer. However, far from the inlet and outlet, the numerical solution is stabilized, and data are extracted with a vertical cut-line through $L/2$. The numerical result for the electric potential is plotted in figure 4.2 together with the analytical expressions. The numerical result agree with the exact Gouy–Chapman solution as expected. This serves as a good verification of both the analytical expression and the numerical set-up.

5 | Microchannel with an ion-selective membrane

Ionic transport through ion-selective membranes is found in a variety of fields from fuel cells to purification of water. This chapter provides a study of electrokinetic effects in a microchannel with an ion-selective membrane, illustrated in figure 5.1, focusing on applications for desalination. An analytical and numerical model of such a system is examined, explaining the effects of *concentration polarization* and *overlimiting* current in an electrolyte in response to an electric field.

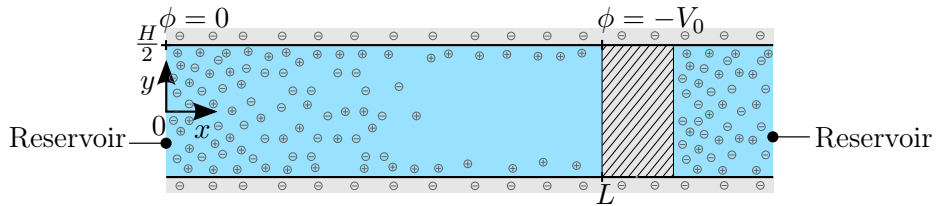


Figure 5.1: Sketch of an electrolyte exhibiting concentration polarization in a microchannel (of height H and length L) with a cation-selective membrane at $x = L$. The reservoirs contain an electrolyte of fixed concentration. An electric potential difference is applied as indicated. Dimensions are for illustrative purpose.

Channel and electrolyte

The reservoirs in figure 5.1 contain a binary 1:1 electrolyte. Of particular importance for desalination, we consider a 1:1 electrolyte of chloride and sodium. The concentration of dissolved salts in seawater is measured by the salinity in units of parts per thousand by weight. The average oceanic salinity is around 35‰. The major constituents are chloride and sodium which account for 30.3‰. This corresponds to a total concentration of chloride and sodium of around 500 mM [11, p. 23-25]. However, since the contributing terms in the ion current density are valid for small ionic concentrations, we adopt the typical concentration $c_0 = 1$ mM used in similar studies [9, 10], which is sufficient for studying some fundamental electrokinetic effects in the system. The reservoirs could be thought of as transverse channels with the electrolyte flowing through. The length of the channel between the reservoir and the membrane is set to $L = 10$ μm , a compromise between demanding sufficiently small concentration gradients near the reservoir and a reasonable computational time. Unless otherwise noticed, the height is set to $H = 1$ μm , which is around the typical height of channels studied for desalination by the group of Henrik Bruus (TMF) at DTU and the group of Martin Bazant at MIT [10].

To drive the ionic transport, an electric potential difference is applied over the system. In the physical set-up this is provided by an anode and a cathode, however, we simply apply this electric potential difference as boundary conditions indicated in figure 5.1.

Ion-selective membrane

A cation-selective membrane is placed in the channel at a distance L from the left reservoir. The membrane could consist of nanochannels with negative charge embedded on the walls. No current of anions can run in the negatively charged nanochannels, however a current of cations can [9]. Due to a high hydraulic resistance in the nanochannels, the velocity of the fluid is approximately zero at the boundary of the membrane.

A physical and chemical study of the membrane is not part of this thesis but has been examined by the TMF group at DTU [12]. We simply apply a boundary condition at the membrane that allows a current of cations but no current of anions.

Physical and chemical considerations

Due to the electric field pointing from left to right, a current of cations flow to the right through the membrane, and a current of anions flow to the left into the reservoir. Since the cation-selective membrane prevents anions from flowing through the membrane from the channel to the right, the anion concentration decreases in front of the membrane. As anions deplete, the electro-neutrality condition causes cations to deplete correspondingly. This creates a longitudinal ionic concentration gradient or so-called concentration polarization with depletion in front of the membrane. We consider the behaviour of the system to the left of the membrane.

Both chemical and physical effects contribute to the ionic current, and in particular to an overlimiting current, explained in section 5.2.1.

Chemical effects include self-ionization of water into hydroxide, OH^- , and hydronium, H_3O^+ . The reaction term in equation (2.15) is non-zero, and hydroxide can effectively circumvent the cation-selective membrane and contribute to the current. Furthermore, the positive space charge formed from depletion of anions lowers the hydronium concentration and increases the hydroxide-concentration correspondingly (pH increases). This reduces the positive space charge, and allows the cation concentration to be higher than zero which further increases the cation current [10]. Of particular importance in microchannels, is the surface effect of a varying surface charge (due to a varying pH) [10]. Surface reactions in the membrane can furthermore lead to "current-induced membrane discharge" and thereby less pronounced concentration polarization [12].

Physical effects in microchannels contributing to the current are the particular important conductive Debye layers near charged walls and advection by electro-osmotic flow.

As a simplified model, we neglect chemical contributions and study only physical effects to provide a thorough understanding of these. In section 5.1, we present a one-dimensional model of the system with uncharged channel walls, and explain the effect of concentration polarization. In section 5.2, we consider charged channel walls which give rise to overlimiting current and an extended depletion region in front of the membrane. The analytical model presented is due to Dydek *et al.* [9].

Results and physical discussions are supported by numerical simulations. Refer to section 5.3 for a description of the numerical set-up. The physical parameters used in the calculations are given in table 5.1.

Quantity	Label	Value
Channel height	H	1 μm
Channel length	L	10 μm
Temperature	T	25 $^{\circ}\text{C}$
Viscosity of water	η	1 mPa s [2, p. 145]
Dielectric constant of water	ϵ	$78\epsilon_0$ [2, p. 147]
Diffusivity of cation	D_+	$1.33 \times 10^{-9} \text{ m}^2 \text{ s}^{-1(a)}$
Diffusivity of anion	D_-	$2.03 \times 10^{-9} \text{ m}^2 \text{ s}^{-1(b)}$
Concentration of ions	c_0	1 mM

Table 5.1: Physical parameters used in the calculations. Diffusivities are for small concentrations of (a) Na^+ and (b) Cl^- in aqueous solutions at temperature 25 $^{\circ}\text{C}$ [2, p. 145].

5.1 Uncharged walls

Neglecting chemical reactions, the continuity equation (2.15) at steady-state becomes in one dimension

$$\partial_x J_{\pm} = 0. \quad (5.1)$$

The ion current densities are thus constant throughout the channel. Notice the huge simplification provided by considering a one-dimensional model. In two dimensions, we cannot simply assume a constant current density for zero divergence since flux can enter and leave a point in infinitely many directions.

As a first approximation, we neglect advection. Since the flow rate depends on the height to the third power for an infinite parallel-plate channel [2, p. 45], this corresponds to sufficiently thin channels where flow is negligible compared to diffusion and transport by the electric field [9]. Thus, the ion current density is given by

$$J_{\pm} = -D\partial_x c_{\pm} \mp c_{\pm} DV_T^{-1} \partial_x \phi. \quad (5.2)$$

We assume that anions and cations have equal diffusivity D . From table 5.1 we notice that this is a fairly good approximation for chloride and sodium dissolved in water.

The ionic species distribute such as to minimize the Coulomb interaction energy, and the electrolyte is assumed charge neutral in equilibrium, $c_{\pm} = c$. This can also be understood by normalizing the one-dimensional Poisson's equation

$$\frac{\partial^2}{\partial \tilde{x}^2} \tilde{\phi} = -\frac{L^2}{2\lambda_D^2} (\tilde{c}_+ - \tilde{c}_-), \quad (5.3)$$

where we have substituted $\phi = V_T \tilde{\phi}$, $c_{\pm} = c_0 \tilde{c}_{\pm}$, and $x = L\tilde{x}$, and used equation (4.5) to introduce the Debye length into the expression. As noted in chapter 4, a typical Debye length is of the order 10 nm, thus $L^2/\lambda_D^2 \gg 1$, and a small difference in concentration induces a large electric field that acts to even out the difference.

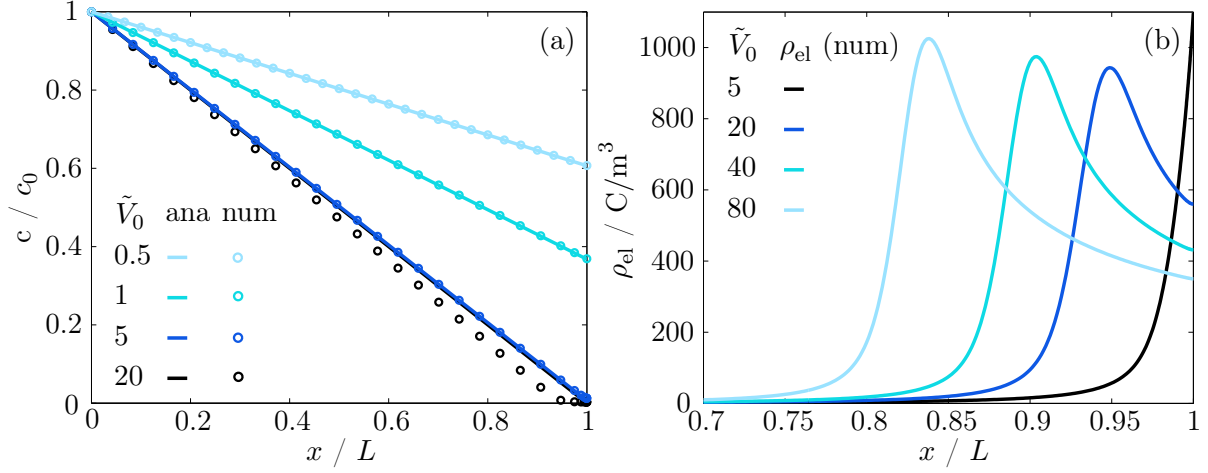


Figure 5.2: Analytical (ana) and numerical (num) calculations of (a) the ionic concentration and (b) electric charge density as function of x for varying electric potential differences in a channel without surface charge.

The cation-selective membrane prevents an anion current in the system

$$J_- = -D\partial_x c + cDV_T^{-1}\partial_x \phi = 0 \quad \Leftrightarrow \quad (5.4a)$$

$$\frac{\partial_x c}{c} = \partial_x \ln(c) = V_T^{-1}\partial_x \phi \quad \Rightarrow \quad (5.4b)$$

$$c = c_0 \exp(\phi/V_T), \quad (5.4c)$$

satisfying the boundary conditions $\phi(0) = 0$ and $c(0) = c_0$ at the inlet.

By inserting equation (5.4c) into the Nernst–Planck equation for the cation current density, we find in normalized form

$$\tilde{J}_+ = -\exp(\tilde{\phi})\partial_{\tilde{x}}\tilde{\phi}, \quad (5.5)$$

where the dimensionless cation current density is defined as $\tilde{J}_+ \equiv J_+L/(2Dc_0)$. Since the cation current density is constant throughout the channel, equation (5.5) is easily integrated

$$\tilde{J}_+\tilde{x} = 1 - \exp(\tilde{\phi}) \quad \Rightarrow \quad (5.6)$$

$$\tilde{J}_+ = 1 - \exp(-\tilde{V}_0), \quad (5.7)$$

satisfying $\tilde{\phi}(0) = 0$, $\tilde{\phi}(1) = -\tilde{V}_0 = -V_0/V_T$. Combining equation (5.4c) and (5.6), we reach the final expression for the concentration

$$c = c_0(1 - \tilde{J}_+\tilde{x}) = c_0 \left[1 - \left(1 - \exp(-\tilde{V}_0) \right) \frac{x}{L} \right]. \quad (5.8)$$

5.1.1 Depletion

The ionic concentration as function of x is plotted in figure 5.2 (a) for varying electric potential differences. The ionic concentration is a linearly decreasing function of x with minimum in

front of the membrane. This effect is referred to as concentration polarization and has great potential for desalination (as we will see in chapter 6).

The concentration gradient yields a diffusive contribution to the cation current density. When the electric potential difference is increased from zero, the cation current density increases as shown in figure 5.3 (a) for $\tilde{\sigma} = 0$, where $\tilde{\sigma}$ is a dimensionless surface charge defined by $\tilde{\sigma} = \sigma / [\text{mC}/\text{m}^2]$. More ions are removed in front of the membrane, and the concentration goes towards zero. The effect is quite strikingly. An electric potential difference of $5V_T$ (0.1 V) yields a concentration of 1% of the inlet concentration in front of the membrane. However, as the concentration goes towards zero in front of the membrane, an even larger electric potential difference cannot increase the cation current further, they would have to move through the charge-neutral region and create an energetically unfavourable space charge region. The ion current is thus limited by the diffusive current which depends linearly on the diffusivity and concentration of the ionic species.

Analytical and numerical calculations agree well for small electric potential differences as seen in figure 5.2 (a). For larger electric potential differences, a space charge region of cations is formed in front of the membrane in the numerical simulations, plotted in figure 5.2 (b) [10]. The energetic cost of forming a space charge region is compensated by the energetic gain when ions are free to lower their electric potential energy, thus the charge-neutrality assumption breaks down. Hence, cations can run through this space charge region and contribute to an overlimiting current as plotted with a dashed line in figure 5.3 (a) (for $\tilde{\sigma} = 0$). However, since it is energetically expensive to form this space charge region, it would benefit greatly to consider charged walls where the Debye screening layer provides the necessary conductive path for overlimiting current.

5.2 Charged walls

Consider a parallel-plate channel with a surface charge $\sigma \leq 0$ on the walls. As explained in chapter 4, cations in the Debye layer screen the negative surface. In the bulk, the ionic species cannot feel the screened surface, here, the electrolyte is assumed charge-neutral. In total, we also require charge-neutrality such that

$$Ze(\langle c_+ \rangle - \langle c_- \rangle)H + 2\sigma = 0 \quad \Leftrightarrow \quad \langle c_+ \rangle = \langle c_- \rangle - \frac{2\sigma}{ZeH}, \quad (5.9)$$

where $\langle c_{\pm} \rangle$ denotes an average concentration along the height H of the channel. The expression to the right in equation (5.9) provides an illustrative picture: In the bulk, the ionic concentrations are equal, and in the Debye layers, cations screen the negatively charged walls and the screening charge is smeared over the height in the one-dimensional model.

The equation for the anion current density is similar to before, thus,

$$\langle c_- \rangle = c_{-,0} \exp(\tilde{\phi}) = c_0 \exp(\tilde{\phi}), \quad (5.10)$$

where c_0 now defines the inlet concentration of anions. Equation (5.9) and (5.10) are inserted

into the Nernst–Planck equation for the cation current density

$$J_+ = -D\partial_x \left[\langle c_- \rangle - \frac{2\sigma}{ZeH} \right] - \left[\langle c_- \rangle - \frac{2\sigma}{ZeH} \right] D\partial_x \tilde{\phi} \quad \Leftrightarrow \quad (5.11a)$$

$$J_+ = -\frac{Dc_0}{L}\partial_{\tilde{x}} \exp(\tilde{\phi}) - \frac{Dc_0}{L} \exp(\tilde{\phi})\partial_{\tilde{x}} \tilde{\phi} + \frac{2D\sigma}{ZeLH}\partial_{\tilde{x}} \tilde{\phi} \quad \Leftrightarrow \quad (5.11b)$$

$$\tilde{J}_+ = -\exp(\tilde{\phi})\partial_{\tilde{x}} \tilde{\phi} + \tilde{\rho}_s \partial_{\tilde{x}} \tilde{\phi}, \quad (5.11c)$$

where $\tilde{\rho}_s \equiv \sigma/(ZeHc_0)$. Equation (5.11c) is easily integrated

$$\tilde{J}_+ \tilde{x} = 1 - \exp(\tilde{\phi}) + \tilde{\rho}_s \tilde{\phi} \quad \Rightarrow \quad (5.12)$$

$$\tilde{J}_+ = 1 - \exp(-\tilde{V}_0) - \tilde{\rho}_s \tilde{V}_0, \quad (5.13)$$

satisfying $\tilde{\phi}(0) = 0$ and $\tilde{\phi}(1) = -\tilde{V}_0$. Note that equation (5.13) reduces to (5.7) for the case of zero surface charge as expected. From equation (5.12) we solve for the potential¹

$$\tilde{\phi} = -W \left(-\frac{\exp((\tilde{J}_+ \tilde{x} - 1)/\tilde{\rho}_s)}{\tilde{\rho}_s} \right) + \frac{\tilde{J}_+ \tilde{x} - 1}{\tilde{\rho}_s}, \quad (5.14)$$

¹Easier to solve if you introduce $g = -\tilde{\phi} + (\tilde{J}_+ \tilde{x} - 1)/\tilde{\rho}_s$

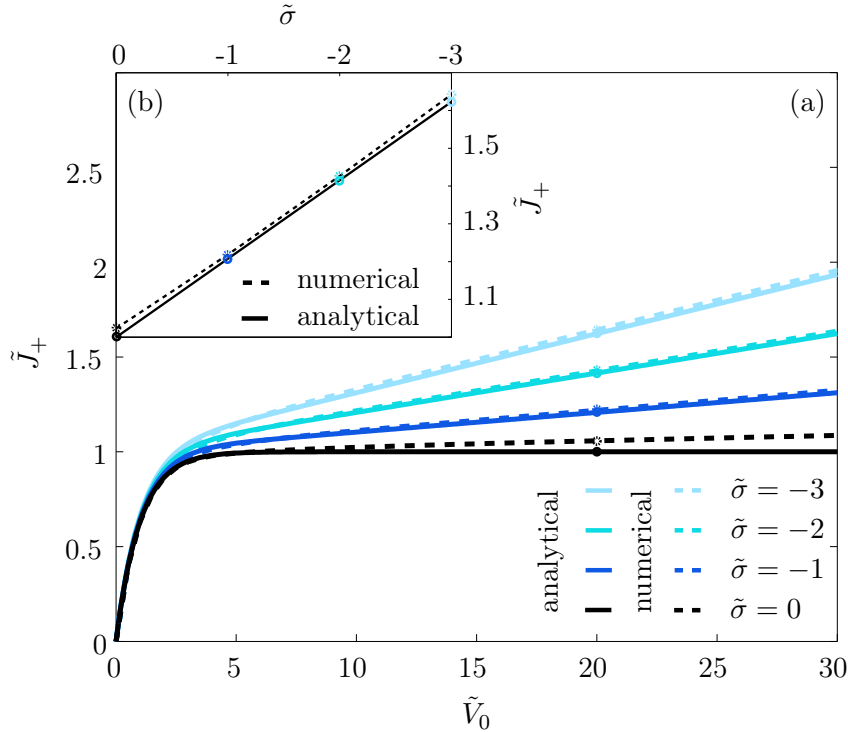


Figure 5.3: Dimensionless cation current density as function of (a) dimensionless electric potential difference for varying wall charges and (b) dimensionless wall charge for an electric potential difference of $20V_T$.

where W is the Lambert W function defined as the inverse of $f(W) = W \exp(W)$. Inserting equation (5.14) in (5.10), we find an expression for the ionic concentrations

$$\langle \tilde{c}_- \rangle = \langle \tilde{c}_+ \rangle + 2\tilde{\rho}_s = \exp \left[-W \left(-\frac{\exp((\tilde{J}_+ \tilde{x} - 1)/\tilde{\rho}_s)}{\tilde{\rho}_s} \right) + \frac{\tilde{J}_+ \tilde{x} - 1}{\tilde{\rho}_s} \right]. \quad (5.15)$$

[9, 10, 13].

5.2.1 Extended depletion region

Analytical and numerical calculations of the dimensionless cation current density is plotted as function of \tilde{V}_0 in figure 5.3 (a) for different wall charges. In figure 5.3 (b), the linear correspondence between cation current density and wall charge as given by equation (5.13) is plotted for $V_0 = 20V_T$.

The conductive Debye layer give rise to an overlimiting current, $1 - \tilde{\rho}_s \tilde{V}_0$. The effect is seen quite clearly in figure 5.4 (b) where numerical simulations of the cation current density (arrow surface in logarithmic scale) and the electric charge density ρ_{el} (color surface) are plotted. In the depleted region, cations run in the Debye layers. Notice that the cation current density vectors point slightly towards the center of the channel just in front of the membrane. This is due to simplified boundary conditions at the membrane as discussed in section 5.3. The effect, however, is exaggerated by the logarithmic scale.

Overlimiting current removes more ions in front of the membrane which leads to an extended depletion region as shown in figure 5.4 (a) where the total ionic concentration (normalized to the inlet concentration) is plotted as function of x for a wall charge of $\sigma = -1 \text{ mC/m}^2$

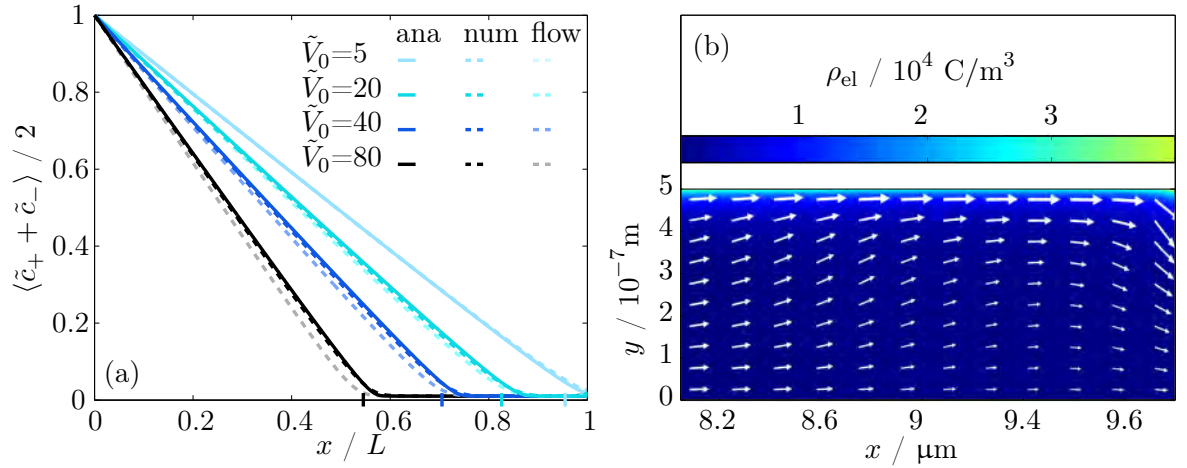


Figure 5.4: (a) Total ionic concentration (normalized to the inlet concentration) as function of x for $\sigma = -1 \text{ mC/m}^2$ and varying electric potential differences. Analytical results are plotted in solid clear colors, numerical results are plotted in similar colors with dashed line. In weak similar colors are plotted the numerical result when flow is considered in the channel (introduced in section 5.4). On the x -axis, the points $x = \tilde{J}_+^{-1}L$ have been marked. (b) Electric charge density (color surface) and cation current density (arrow surface in logarithmic scale) for $\sigma = -1 \text{ mC/m}^2$ and $V_0 = 20V_T$.

and varying electric potential differences. In the linear regime of the concentration profile $c_+ \approx c_- = c$, thus, the total ion current density is

$$J_+ + J_- = J_+ = -2D\partial_x c, \quad (5.16a)$$

and is dominated by diffusion. Changing to dimensionless variables we find by straightforward integration

$$\tilde{c} = 1 - \tilde{J}_+ \tilde{x}, \quad (5.17)$$

satisfying $\tilde{c}(0) = 1$. This elucidates the important scaling characteristic of the depletion region. The extend of the depletion region, approximately equal to $(1 - \tilde{J}_+^{-1})L$, scales linearly with the length of the channel [9, 10]. In figure 5.4 (a), the points $x = \tilde{J}_+^{-1}L$ are marked on the x -axis and show good agreement with the extend of the depletion region.

5.3 Numerical set-up

In the previous sections, analytical expressions have been compared to numerical calculations. The numerical set-up is illustrated in figure 5.5.

The governing equations are similar to the system described in chapter 4. New physics lies in the boundary conditions.

Electric potential

The Gouy–Chapman solution (4.14) added an external electric potential difference is applied as constraints

$$\phi(y) = 4V_T \operatorname{arctanh} \left[\tanh \left(\frac{\zeta}{4V_T} \right) \exp \left(-\frac{(H/2 - y)}{\lambda_D} \right) \right], \quad (5.18)$$

for $y \in \{\partial\Omega_1\}$, and

$$\phi(y) = 4V_T \operatorname{arctanh} \left[\tanh \left(\frac{\zeta}{4V_T} \right) \exp \left(-\frac{(H/2 - y)}{\lambda_D^*} \right) \right] - V_0, \quad (5.19)$$

for $y \in \{\partial\Omega_4\}$. These expressions depend on the ionic concentration infinitely far from the charged wall via the Debye length λ_D . At the inlet, we set this concentration to c_0 . However,

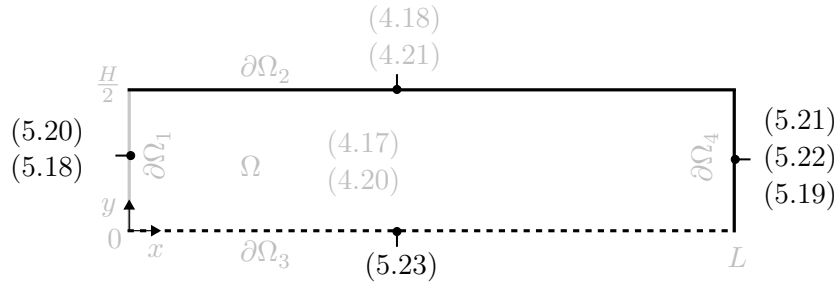


Figure 5.5: Schematic illustration of the numerical set-up of a microchannel with a cation-selective membrane. The rigid wall $\partial\Omega_2$ and membrane $\partial\Omega_4$ are drawn in black, the inlet $\partial\Omega_1$ is drawn in grey, and the symmetry line $\partial\Omega_3$ is drawn in dashed black. Numbers in parenthesis refer to the equation number of the governing equation or boundary condition. Numbers in black are new for this system, numbers in grey are similar to the system in figure 4.3.

the condition at the membrane is not as simple to implement. We use a boundary probe to measure the concentration at the symmetry line $\partial\Omega_3$ where $c_+ \approx c_-$. Note from figure 5.4 (b) that this condition yields a slightly higher electric charge density near the membrane, which allows the cation current density to go slightly down into the channel just in front of the membrane. However, the effect is quite small, and the numerical and analytical results show very good agreement in figure 5.4 (a).

Simulations are run for varying wall charge σ on the rigid wall $\partial\Omega_2$ through the weak contribution (4.21).

Ionic concentration

The concentration at the inlet is set to the Gouy–Chapman solution (4.2) as a constraint

$$c_{\pm}(y) = c_0 \exp\left(\mp 4 \operatorname{arctanh}\left[\tanh\left(\frac{\zeta}{4V_T}\right) \exp\left(-\frac{(H/2 - y)}{\lambda_D}\right)\right]\right), \quad (5.20)$$

for $y \in \{\partial\Omega_1\}$.

A discussion of the weak contribution for the ion current densities is provided in the following section.

5.3.1 Ion current density at the membrane

The cation-selective membrane prevents anion current through the membrane, hence, we apply the weak contribution

$$\mathbf{n} \cdot \mathbf{J}_-(\mathbf{r}) = 0, \quad (5.21)$$

for $\mathbf{r} \in \{\partial\Omega_4\}$.

When an electric potential difference is applied, the cation concentration decreases in front of the membrane. Inside the membrane, the cation concentration is high such as to satisfy charge-neutrality (remember the membrane consists of negatively charged nanochannels). This behaviour is modelled by setting $\partial_x c_+ = 0$ in the weak contribution for the Nernst–Planck equation

$$\mathbf{n} \cdot \mathbf{J}_+(\mathbf{r}) = -D_+ n_y \partial_y c_+(\mathbf{r}) - c_+(\mathbf{r}) D_+ V_T^{-1} \mathbf{n} \cdot \nabla \phi(\mathbf{r}), \quad (5.22)$$

for $\mathbf{r} \in \{\partial\Omega_4\}$.

For the real physical set-up, this condition is not a complete description of the behaviour at the boundary between the channel and the membrane. The contributing terms in the right-hand side of equation (5.2) for the cation current density are large compared to the current density (which remain constant) due to the large gradients at the interface. Thus, similar to the behaviour of an electrolyte near a charged surface, the concentration is governed by Boltzmann statistics which yields a small but finite transition region between low and high concentrations at the interface [10]. Thus, the condition $\partial_x c_+ = 0$ is satisfied close to the membrane, but not exactly at the interface. If we regard the boundary at L , not as the membrane, but as a point close to the membrane, the numerical model describes the system correctly. Things complicate slightly when flow is introduced.

5.3.2 Symmetry and technical aspects

In order to reduce computational time, we take advantage of the horizontal symmetry line through the center of the channel and simulate only half of the system. At the symmetry line, the normal component of the gradient of all dependent variables must be zero, i.e. flux does not enter from a part of the system into its symmetric part. We collect this requirement for all dependent variables into

$$\mathbf{n} \cdot \text{flux}(\mathbf{r}) = 0, \quad (5.23)$$

for $\mathbf{r} \in \{\partial\Omega_3\}$.

For computational reasons, we define two new dependent variables

$$\hat{c}_{\pm} = \ln \left(\frac{c_{\pm}}{c_0} \right) \quad \Leftrightarrow \quad c_{\pm} = c_0 \exp(\hat{c}_{\pm}). \quad (5.24)$$

In this way, the problem of searching for concentrations near zero is transformed into a problem of searching for large negative values of \hat{c}_{\pm} , which is preferred by COMSOL.

In order to run simulations in the highly non-linear regime of large electric potential differences, we run a parametric sweep with increasing V_0 . In this way, COMSOL uses the previous solution as input for the next simulation. However, since often COMSOL do not let solutions converge properly between steps in a single-parameter sweep, we define a dummy parameter to run over the same values as V_0 [10].

The concentration profile in figure 5.4 (a) is calculated using a linear projection operator in COMSOL.

5.4 Flow

In general, it is difficult to find analytical solutions to the non-linear Navier–Stokes equation, and often one have to rely on numerical methods. However, some idealized flow solutions exist, and they provide an important physical insight. This chapter introduces the steady-state cases of Poiseuille-flow and electro-osmotic flow.

Consider a translational invariant section of the channel in figure 5.1 far from the membrane. When an external electric potential difference is applied, the Debye layers are brought to move in response to the body force density $-\rho_{\text{el}}^{\text{eq}} \nabla \phi_{\text{ext}}$, where $\rho_{\text{el}}^{\text{eq}} = -\epsilon \partial_y^2 \phi_{\text{eq}}$ and ϕ_{eq} is given by the Gouy–Chapman solution (4.14) or the Debye–Hückel approximation (4.7). When the electrolyte is brought to move, the membrane provides a backpressure. In steady-state, the Navier–Stokes equation used for analyzing this flow is

$$\rho(\mathbf{v} \cdot \nabla) \mathbf{v} = -\nabla p + \eta \nabla^2 \mathbf{v} - \rho_{\text{el}}^{\text{eq}} \nabla \phi_{\text{ext}}. \quad (5.25)$$

The non-linear left-hand side might vanish due to symmetry or by assumption of sufficiently low Reynolds numbers. In the numerical set-up, we make the last assumption. However, for the simple geometry considered here (far from the membrane), due to constant pressure- and

electric potential gradients (approximately true for sufficiently low electric potential differences) and vanishing forces in the y -direction, the velocity is independent of x with only the x -component being non-zero. Hence $(\mathbf{v} \cdot \nabla)\mathbf{v} = 0$, and equation (5.25) simplifies to

$$0 = \eta \partial_y^2 v_x(y) - \frac{\Delta p}{L} + \epsilon (\partial_y^2 \phi_{\text{eq}})(y) \frac{-V_0}{L}, \quad (5.26)$$

satisfying $p(0) = 0$, $p(L) = \Delta p$, $\phi_{\text{ext}}(0) = 0$, and $\phi_{\text{ext}}(L) = -V_0$.

We make the ansatz $v_x(y) = v_{x,1}(y) + v_{x,2}(y)$

$$0 = \left[\eta \partial_y^2 v_{x,1}(y) - \frac{\Delta p}{L} \right] + \left[\eta \partial_y^2 v_{x,2}(y) + \epsilon (\partial_y^2 \phi_{\text{eq}})(y) \frac{-V_0}{L} \right], \quad (5.27)$$

and solve the two terms separately. From the first term, we find

$$v_{x,1}(y) = - \left[(H/2)^2 - y^2 \right] \frac{1}{2\eta} \frac{\Delta p}{L}, \quad (5.28)$$

satisfying $v_{x,1}(\pm H/2) = 0$. This solution is a standard Poiseuille flow.

In the second term, we insert the solution to equation (4.6) for the equilibrium Debye–Hückel potential and find

$$v_{x,2}(y) = \left[1 - \frac{\cosh\left(\frac{y}{\lambda_D}\right)}{\cosh\left(\frac{H}{2\lambda_D}\right)} \right] \frac{\epsilon \zeta - V_0}{\eta L}, \quad (5.29)$$

satisfying $\phi(\pm H/2) = \zeta$ and $v_{x,2}(\pm H/2) = 0$. This is the electro-osmotic flow due to movement of the Debye layers in response to an electric field [2, ch. 9]. We consider the behaviour of the total electro-osmotic flow with backpressure further after introducing the numerical set-up.

5.4.1 Numerical set-up

The numerical set-up is illustrated in figure 5.6. Boundary conditions applied for the pressure and velocity fields are given in table 5.2.

Velocity

At steady state and for low Reynolds number, the Navier–Stokes equation becomes

$$\nabla \cdot \boldsymbol{\sigma} = -\mathbf{f}. \quad (5.30)$$

For an incompressible fluid, the components of the stress tensor $\boldsymbol{\sigma}$ are given by

$$\sigma_{ij} = -p\delta_{ij} + \eta(\partial_j v_i + \partial_i v_j), \quad (5.31)$$

and the body force density comprises the electrostatic force density

$$\mathbf{f} = -\rho_{\text{el}} \nabla \phi = -Ze(c_+ - c_-) \nabla \phi. \quad (5.32)$$

In weak form equation (5.30) becomes

$$\int_{\partial\Omega} da v_{i,n} \mathbf{n} \cdot \boldsymbol{\sigma}_i + \int_{\Omega} d\mathbf{r} [-\nabla v_{i,n} \cdot \boldsymbol{\sigma}_i + v_{i,n} f_i] = 0, \quad (5.33)$$

where the dependent variables are the x -component and y -component of the velocity field.

We require normal inflow (5.36) (table 5.2) and translational invariance (5.37) at the inlet. At the symmetry line, we apply the usual no-flux condition (5.23) and in addition, we require that the normal component of the velocity field is zero (5.40) since otherwise opposite pointing velocity vectors would be at the same point in space.

At the walls and membrane, we assume no-slip boundary conditions (5.39). This is due to the assumption of momentum relaxation between the fluid molecules in contact with the wall [2, p. 37]. Note that when we introduced the boundary condition $\partial_x c_+ = 0$ at the membrane in section 5.3.1, we made clear, that this described the system till very close to the membrane. When the velocity field is introduced, this boundary condition becomes an approximation since we assume a no-slip condition to characterize the flow near the membrane. Thus, we should not overinterpret results very close to the membrane.

Pressure

For an incompressible fluid, the continuity equation reads

$$\nabla \cdot \mathbf{v} = 0. \quad (5.34)$$

We could write this in the usual weak form, but since we already deal with derivatives of the velocity field in the Navier–Stokes equation, we simply write it in the form

$$\int_{\Omega} d\mathbf{r} p_n \nabla \cdot \mathbf{v} = 0, \quad (5.35)$$

where p_n are test-functions for the pressure [6]. Note that even though equation (5.34) do not involve the pressure explicitly, it is coupled into the velocity via the full stress tensor in (5.33).

The charged walls provide an electrostatic pressure (5.38).

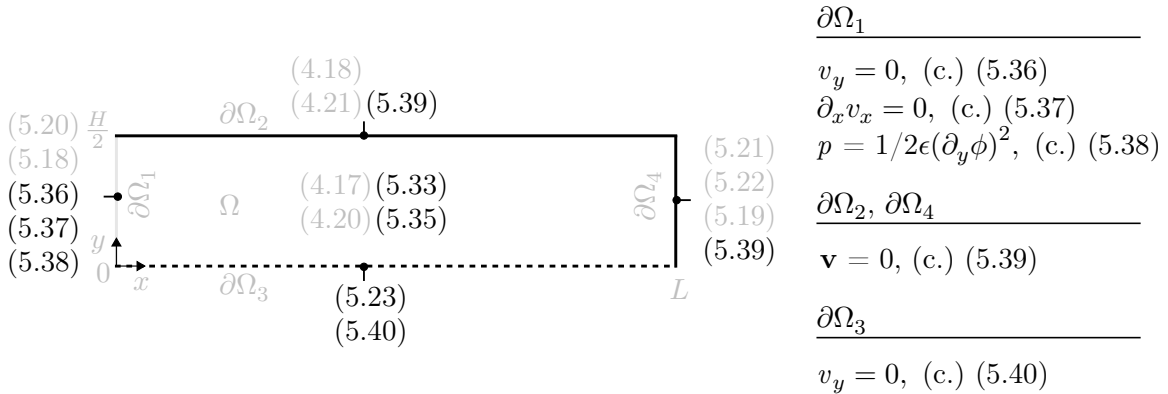


Figure 5.6: Schematic illustration of the numerical set-up of a channel with a cation-selective membrane including pressure and velocity fields. The rigid wall $\partial\Omega_2$ and membrane $\partial\Omega_4$ are drawn in black, the inlet $\partial\Omega_1$ is drawn in grey, and the symmetry line $\partial\Omega_3$ is drawn in dashed black. Numbers in parenthesis refer to the equation number of the governing equation or boundary condition. Numbers in black are new for this system, numbers in grey are similar to the system in figure 5.5.

Table 5.2: Additional boundary conditions applied for the pressure and velocity fields. Note that additional boundary conditions at the symmetry line are governed by (5.23). (c.) denotes constraint.

5.4.2 Results

In figure 5.7 (b), the magnitude of the velocity field (color surface) and velocity field vectors (arrow surface) are plotted near the membrane for $\sigma = -1 \text{ mC/m}^2$ and $V_0 = 5V_T$. The electrolyte is dragged by the Debye layer near the channel walls and flows back in the center of the channel due to the backpressure provided by the membrane. Near the membrane, a vortex is formed. As we will see, this becomes important when we study a desalination device in chapter 6.

In the full system, the pressure and electric potential are not simple linear functions of x . However, for sufficiently small electric potential differences, they are approximately linear. For $V_0 = 0.1V_T$, the pressure difference over the channel is $\Delta p = 0.3 \text{ Pa}$. The analytical solution for the x -component of the velocity field is plotted in figure 5.7 (a) together with the numerical result at a cut line through the channel at $x = 0.3L$. The analytical and numerical results show fine agreement.

As seen in figure 5.7 (c), electrolyte of high ionic concentration flows near the charged wall towards the membrane and desalinated electrolyte flows back in the center of the channel. This provides a transverse concentration gradient in addition to the longitudinal concentration gradient covered by the analytical model. Furthermore it gives rise to the question: Can we extract the most desalinated electrolyte flowing in the center of the channel when electrolyte of higher ionic concentration flows near the walls? In chapter 6, we return to a discussion of how this transverse concentration gradient affects desalination.

The ionic concentration (averaged over the height of the channel and normalized to the inlet concentration) for a channel with $\sigma = -1 \text{ mC/m}^2$ is plotted in figure 5.4 (a) together with analytical and numerical concentration profiles for the system without flow for varying electric potential differences. We see that the electro-osmotic flow with backpressure does not affect the average concentration profile remarkably since the total advective current is small. As expected, charged walls still provide an extended depletion region in the system, the extend being illustrated in figure 5.7 (d), where the total ionic concentration (normalized to the inlet concentration) is plotted as a function of x for different wall charges and electric potential differences.

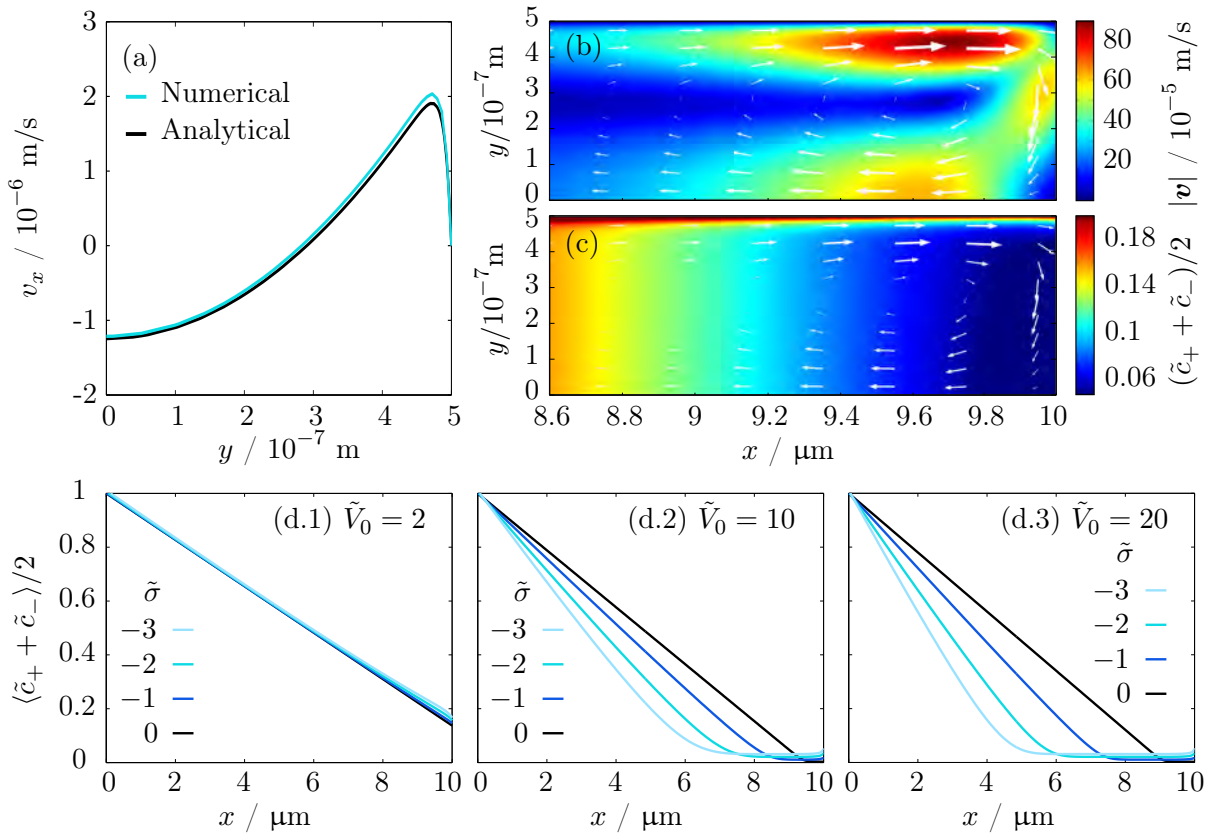


Figure 5.7: (a) Numerical and analytical calculations of v_x as function of y for a vertical cut line through the channel at $x = 0.3L$ for $\sigma = -1 \text{ mC/m}^2$ and $V_0 = 0.1V_T$. (b) Magnitude of velocity field (color surface) and velocity field vectors (arrow surface) near the membrane for $\sigma = -1 \text{ mC/m}^2$ and $V_0 = 5V_T$. (c) Total ionic concentration relative to c_0 (color surface) and velocity field vectors (arrow plot) near the membrane for $\sigma = -1 \text{ mC/m}^2$ and $V_0 = 5V_T$. (d) Total ionic concentration (averaged over the height of the domain and normalized to the inlet concentration) as function of x for varying wall charge and an electric potential difference of $V_0 = 2V_T$ (d.1), $V_0 = 10V_T$ (d.2), and $V_0 = 20V_T$ (d.3).

6 | Desalination

Many possible electrokinetic systems for desalination devices have been suggested. The specific configuration vary, however, common for the systems studied by the group of Henrik Bruus (TMF) at DTU and the group of Martin Bazant at MIT are the components illustrated in figure 6.1 (a) [14, 10].

The device is composed of an anode and a cathode to drive the ionic transport, an ion-selective membrane to develop concentration polarization, and a porous glass frit to provide extended depletion (the glass spheres provide a negative surface charge). The porous glass frit is an inexpensive alternative to precise microfabrication of channels. Numerous channels are effectively formed in the frit (illustrated with a dashed line in figure 6.1 (a)), and the porous structure ensures that desalinated water can be extracted. The frit also protects the membrane from fouling, and is easy to clean or cheap to replace, rather than replacing the membrane if fouled [14].

In this chapter, we consider the system established in chapter 5 with outlet channels implemented in front of the membrane, as illustrated in figure 6.1 (b). This provides a simple model of a single channel formed in the glass frit where an outflow is allowed in front of the membrane. The channels formed in the frit have a complex form, but for simplicity we

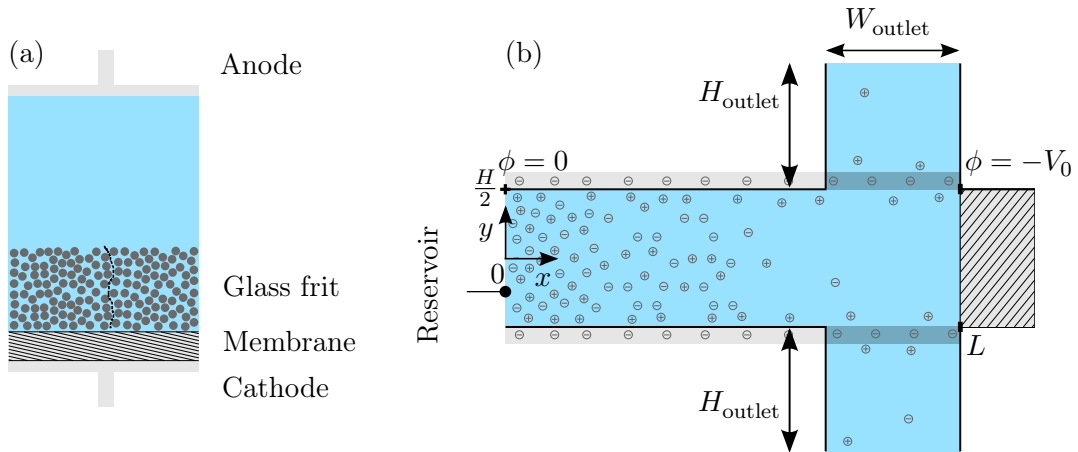


Figure 6.1: (a) Illustration of the components used in the desalination devices studied by the group of Henrik Bruus at DTU and the group of Martin Bazant at MIT. Inspiration to drawing from [10]. (b) Illustration of the suggested model of the microchannels formed in the glass frit.

consider a two-dimensional parallel plate channel. In the porous glass frit, we expect the conductive path in the Debye layers, contributing to an overlimiting current, to effectively remain to the membrane, with electrolyte escaping through holes in the porous channel. In order to model the porous structure of the channel wall, we implement a *leaky* wall in front of the outlet channel ($\partial\Omega_5$ in figure 6.2) [13]. The leaky wall maintains the same surface charge σ as the remaining wall but allows electrolyte to flow through.

Similar studies often take a macroscopic approach and neglect electro-osmotic flow [15]. As we saw in chapter 5, electrolyte of high concentration flows near the charged channel walls, and it is not a trivial question whether we can actually extract the desalinated water flowing in the center of the channel. The advantage of this model is that we can get an understanding of some of the effects contributing in the microchannels formed in the glass frit, and how flow in these affects desalination. In particular, we study whether we can exploit the extended depletion region provided by charged channel walls.

6.1 Symmetric wall charge

The numerical set-up is illustrated in figure 6.2. Additional boundary conditions applied for the outlet channel and the leaky wall are given in table 6.1. A comment is in order for some of the boundary conditions.

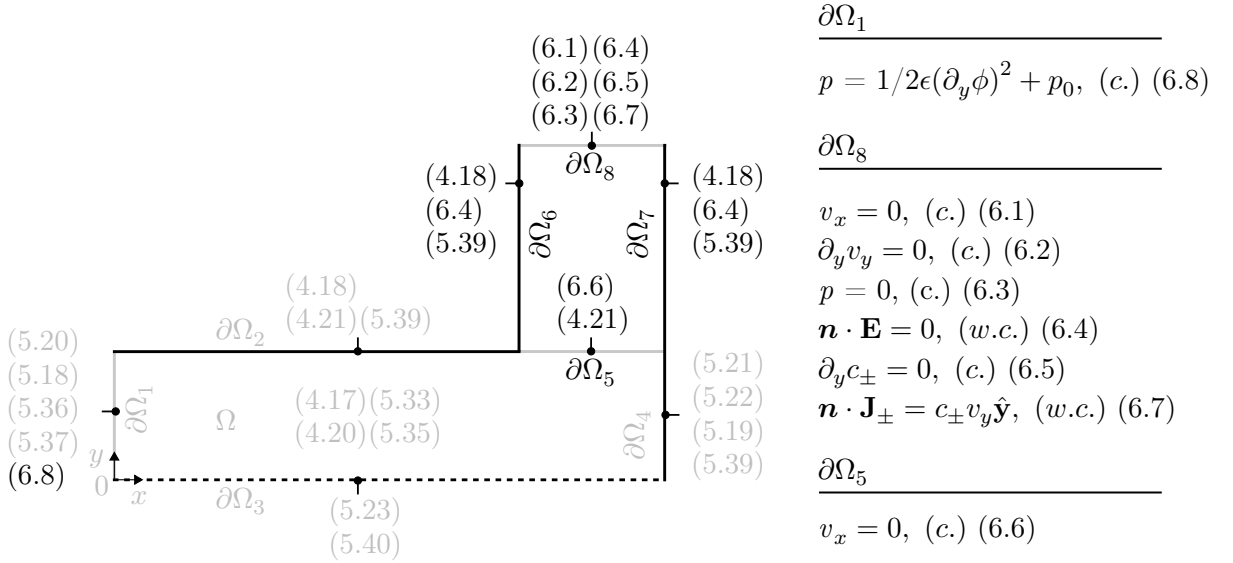


Figure 6.2: Schematic illustration of the numerical set-up of a desalination device with symmetrically charged walls. The rigid walls $\partial\Omega_2$, $\partial\Omega_6$, $\partial\Omega_7$, and membrane $\partial\Omega_4$ are drawn in black, the inlet $\partial\Omega_1$, outlet $\partial\Omega_8$, and leaky wall $\partial\Omega_5$ are drawn in grey, and the symmetry line $\partial\Omega_3$ is drawn in dashed black. Numbers in parenthesis refer to the equation number of the governing equation or boundary condition. Numbers in black are new for this system, numbers in grey are similar to the system in figure 5.6.

Table 6.1: Additional boundary conditions applied to the leaky wall and outlet channel. (c.) denotes constraint and (w.c.) denotes weak contribution.

The leaky wall maintains the same charge as the remaining wall, governed by the weak contribution (4.21). This lowers the zeta-potential but conserves the total space charge in the two Debye layers formed on each side of the leaky wall. The surface charge must be embedded into a wall, thus we require zero tangential velocity.

For the pressure we apply the constraint $p = 1/2\epsilon(\partial_y\phi)^2 + p_0$ at the inlet $\partial\Omega_1$ and $p = 0$ at the outlet $\partial\Omega_8$. In the system with the glass frit, the pressure at the outlet would depend on the next formed channel, however, it is difficult to determine this pressure, and the condition of zero external pressure is sufficient for our study. Nevertheless, some of the observations in the following are indeed due to this assumption.

The concentration in the outlet channel is approximately independent of y , hence, we apply the constraint $\partial_y c_{\pm} = 0$ at the outlet. However, numerical simulations can be tricky and in order for COMSOL to accept this constraint, we apply in addition the weak contribution $\mathbf{n} \cdot \mathbf{J}_{\pm} = c_{\pm} v_y$.

The normal component of the electric field is set to zero at the outlet. We do not consider charged walls in the outlet channel, and do not apply a potential difference on the walls, but simply treat the outlet channel as a confinement for the electrolyte outflow.

For the numerical simulations, unless otherwise noted, $H_{\text{outlet}} = 3H$ (the length of $\partial\Omega_6$ and $\partial\Omega_7$), $W_{\text{outlet}} = H$ (the length of $\partial\Omega_5$ and $\partial\Omega_8$), and physical parameters are as given in table 5.1.

6.1.1 Mesh and mesh convergence

The mesh is constructed as described in table 6.2 for $d_{\text{mesh}} = 5$ nm.

Domain/ boundary	Mesh
Ω	Maximum element size $20d_{\text{mesh}}$.
$\partial\Omega_2$	Boundary layer, thickness $1/5d_{\text{mesh}}$ (8 layers with stretching factor 1.2). Maximum element size $3/2d_{\text{mesh}}$.
$\partial\Omega_5$	Maximum element size d_{mesh} .
$\partial\Omega_4, \partial\Omega_8$	Maximum element size $6d_{\text{mesh}}$.
$\partial\Omega_2, \partial\Omega_6$	Corner refinement on corner between $\partial\Omega_2$ and $\partial\Omega_6$.

Table 6.2: Specification of the mesh used in the numerical simulations of the channel with symmetrically charged walls.

In order to resolve fields from the Debye layer varying in the direction normal to the wall $\partial\Omega_2$, on a length scale around 10 nm, we apply boundary layers. To resolve the tangential varying fields, we apply in addition a maximum element size of $3/2d_{\text{mesh}}$. At the leaky wall we have both considerable normal and tangential varying fields, therefore, we do not use boundary layers but implement a finer maximum element size.

Note that for a 1:1 electrolyte of ionic concentration around 250 mM (of both anions and cations, as for seawater), the Debye length becomes 0.61 nm (for $T = 25$ °C), and we would

have to optimize the mesh or geometry in order to resolve these fields, especially at points between boundaries (as the point between $\partial\Omega_5$ and $\partial\Omega_8$).

For the results in figure 6.5, we have used a coarser mesh without boundary layers in order to calculate the average concentration (linear extrusion in COMSOL does not work with boundary layers). The fields have been compared with results from simulations with the finer mesh and agree.

For verification of the numerical results, we perform a mesh convergence analysis (refer to section 3.2). The reference solution is found for $d_{\text{mesh}} = 5$ nm. The relative convergence parameter C (3.8) for v_x , p , ϕ , and c_+ is plotted in figure 6.3 for $V_0 = 20V_T$, (a) $\sigma = 0$ C/m², (b) $\sigma = -1$ mC/m², and varying d_{mesh} . v_y and c_- are left out from the graph since these lie very close to the curves for v_x and c_+ , respectively.

From the semilogarithmic plot we see an exponential convergence of all fields. Note that the pressure and velocity fields have a higher relative convergence parameter since their governing equations deal with derivatives of the velocity.

For the simulations, we have used the smallest d_{mesh} possible on the student terminals provided by DTU. If time allowed, it would be worth the effort to optimize the mesh and do simulations on a more powerful computer.

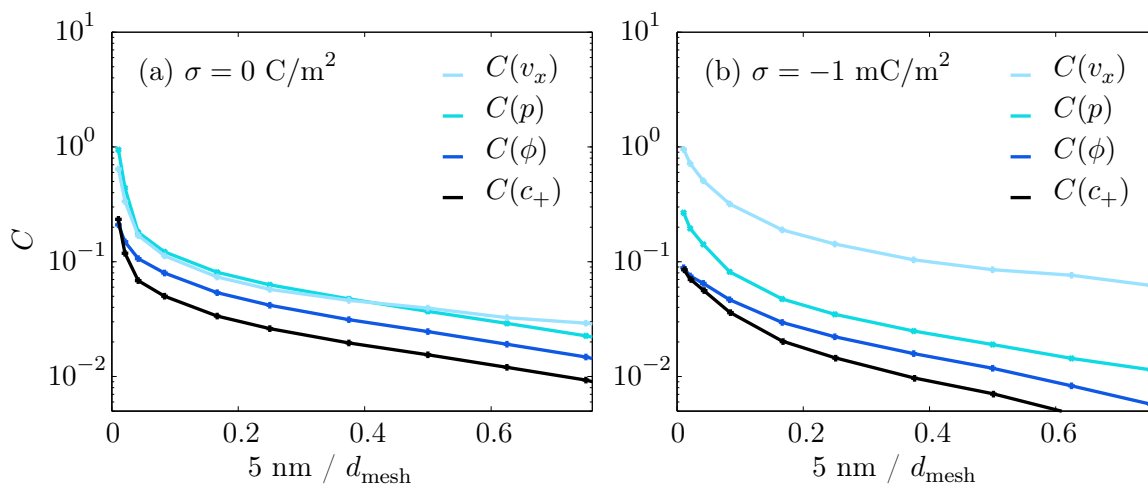


Figure 6.3: Mesh convergence analysis for $V_0 = 20V_T$ and (a) $\sigma = 0$ C/m², and (b) $\sigma = -1$ mC/m². The relative convergence parameter C for v_x , p , ϕ , and c_+ is plotted for varying d_{mesh} .

6.1.2 Results

The ionic concentration of extracted electrolyte, denoted outlet concentration c_{outlet} , is calculated by

$$c_{\text{outlet}} = \frac{\int_{\partial\Omega_8} dx(c_+ + c_-)v_y}{\int_{\partial\Omega_8} dxv_y}. \quad (6.9)$$

The outlet concentration relative to the inlet concentration $\tilde{c}_{\text{outlet}}$ is plotted in figure 6.4 as function of area flow rate $Q = 2 \int_{\partial\Omega_8} dxv_y$ for (a) $p_0 = 0$ Pa, (b) $p_0 = 10^3$ Pa, and varying σ .

For $p_0 = 0$ Pa and $V_0 = 20V_T$, the outlet concentration is only a few percent of the inlet concentration, thus desalination is indeed accomplished. For even higher electric potential differences, we find the relative outlet concentration down to around 10^{-4} for $\sigma = 0$ C/m². From figure 6.4 (b) for $V_0 = 0V_T$, we find that a pressure difference of $\Delta p = 10^3$ Pa yields a flow rate around 6.9×10^{-9} m²s⁻¹ to 7.4×10^{-9} m²s⁻¹. To obtain a similar flow rate for the purely electro-osmotic driven system, we should apply an electric potential difference of the order $70V_T$ to $90V_T$ (1.8 V to 2.3 V). This will give us a relative outlet concentration in the range 4×10^{-3} to 10^{-4} .

Notice that even for zero wall charge, a quite large flow is achieved when an electric potential difference is applied. A pressure is build up in front of the membrane due to the space charge region formed as shown in figure 5.2 (b). This drives a flow towards the outlet which is the nearest boundary condition with $p = 0$ Pa.

The specific behaviour of figure 6.4 is due to a combination of various effects in the non-linear system. In the following, we provide a discussion of the results. For the discussion, refer to figure 6.5 of (a) the velocity field for the system with $\sigma = -1$ mC/m² and (b) the total concentration $\langle \tilde{c}_+ + \tilde{c}_- \rangle / 2$, averaged over the height of the main channel and normalized to the inlet concentration, as function of x for (1) $V_0 = 2V_T$, (2) $V_0 = 20V_T$, and (3) $V_0 = 35V_T$.

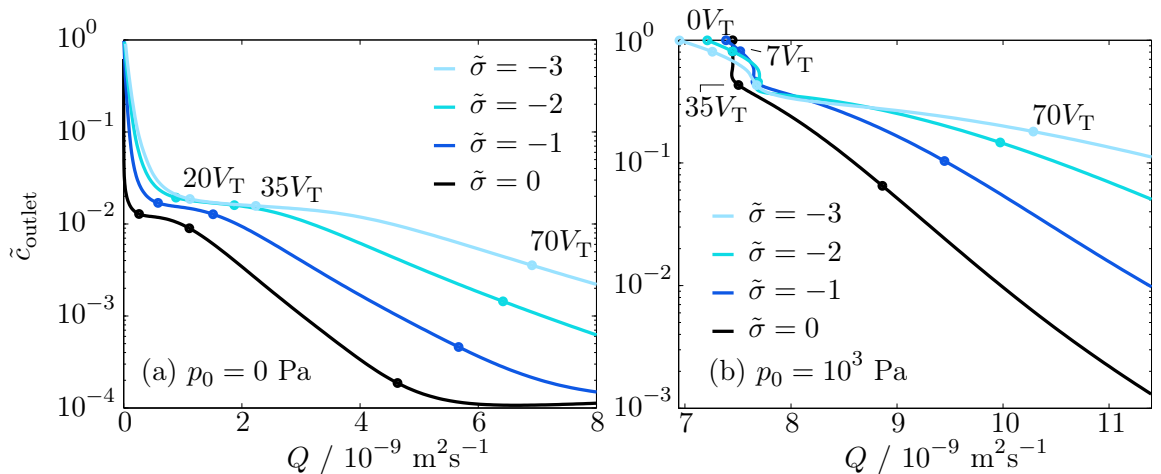


Figure 6.4: Total ionic concentration of extracted electrolyte relative to the concentration at the inlet as function of flow rate with (a) no external pressure applied, and (b) an external pressure difference of $p_0 = 10^3$ Pa. Some corresponding electric potential differences are marked on the curves.

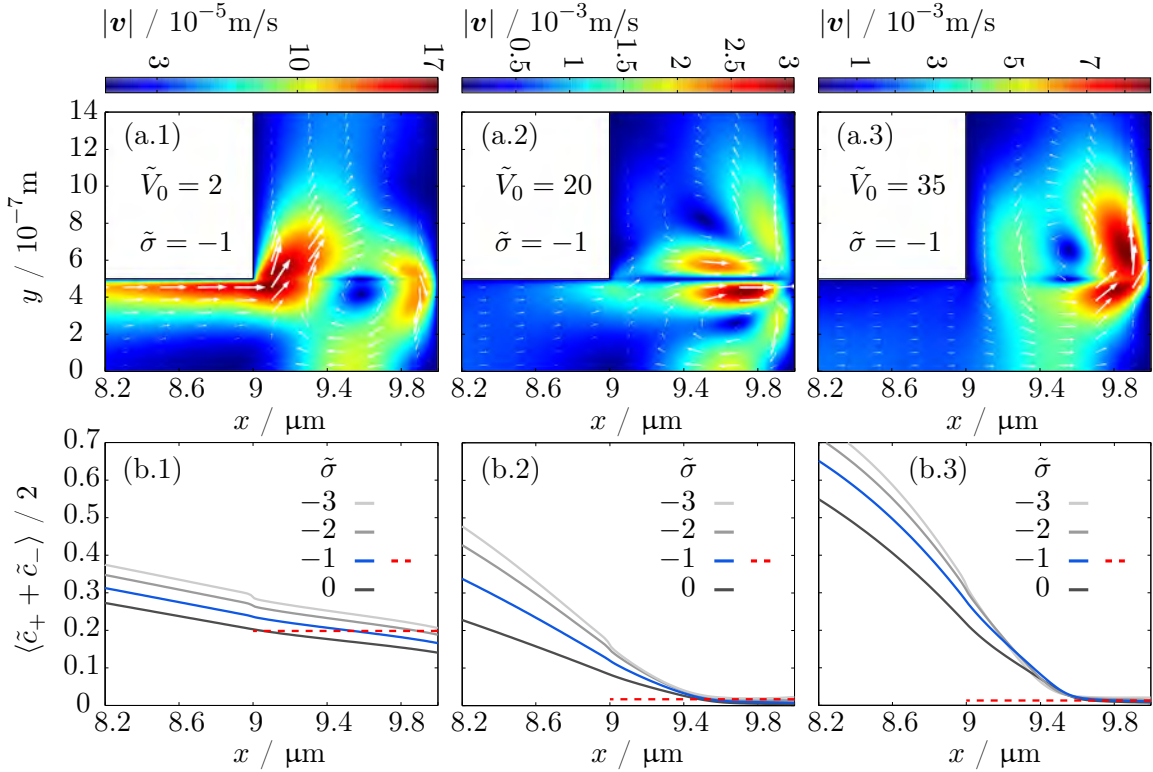


Figure 6.5: (a) Magnitude of velocity field (color surface) and velocity field vectors (arrow surface) near the outlet channel for $\sigma = -1$ mC/m² and (1) $V_0 = 2V_T$, (2) $V_0 = 20V_T$, and (3) $V_0 = 35V_T$. (b) Total ionic concentration (averaged over the height of the main channel and normalized to the inlet concentration) as function of x near the outlet channel for varying wall charges and (1) $V_0 = 2V_T$, (2) $V_0 = 20V_T$, and (3) $V_0 = 35V_T$. The outlet concentration for $\sigma = -1$ mC/m² is shown with a red dashed line.

As the electric potential difference is increased from zero, the outlet concentration decreases as the concentration in front of the outlet channel starts to decrease. From figure 6.5 (a.1) we see that a vortex is formed due to the electro-osmotic flow and backpressure from the membrane. For small electric potential differences, overlimiting current does not have a pronounced effect, and the higher ionic concentration near charged walls dominates as seen in figure 6.5 (b.1) (in agreement with figure 5.7 (d.1)). The electrolyte is flushed out from a broad part of the width of the outlet channel, and the relative outlet concentration (0.199 for the situation in figure 6.5 (b.1), illustrated with a red dashed line) is only slightly above the average concentration in front of the outlet channel (0.197). The outlet concentration is slightly larger since the largest velocity field area, flushing out electrolyte to the outlet, is nearer to the charged wall than the center of the main channel.

As we increase the electric potential difference, we still find that a smaller wall charge provides better desalination for a given flow rate and electric potential. From the physical discussion in chapter 5, we would expect the opposite result. Nevertheless, this result has also been observed in similar studies [13]. However, in the following we provide an explanation of this observation. The reason is found in figure 6.5 (b). We observe that charged walls do not contribute to an extended depletion region in the system, thus we find a higher outlet

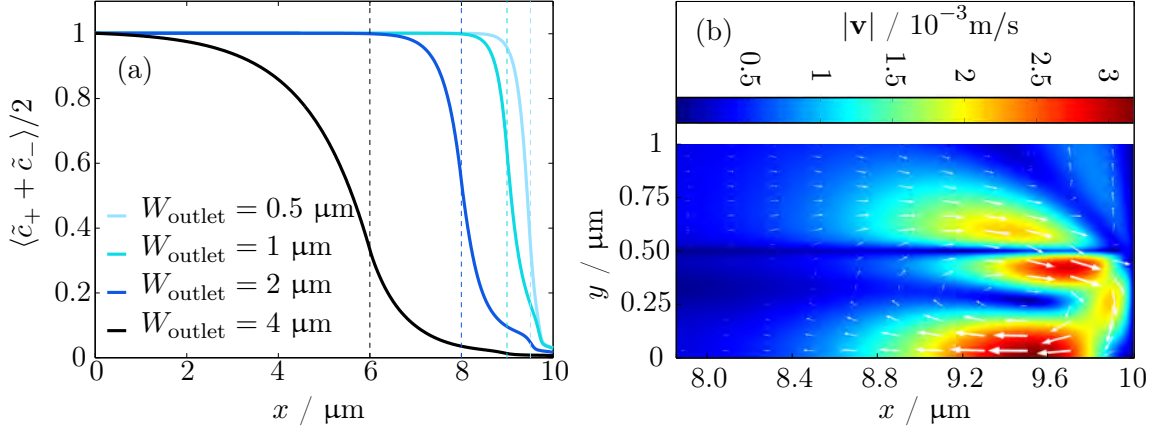


Figure 6.6: (a) Total ionic concentration (averaged over the height of the main channel and normalized to the inlet concentration) as function of x for $\sigma = -1 \text{ mC/m}^2$, $p_0 = 0 \text{ Pa}$, $V_0 = 100V_T$ and varying width of the outlet channel, marked with a dashed line. (b) Magnitude of velocity field (color surface) and velocity field vectors (arrow surface) near the membrane for $\sigma = -1 \text{ mC/m}^2$, $p_0 = 0 \text{ Pa}$, $V_0 = 20V_T$, and $W_{\text{outlet}} = 4 \mu\text{m}$.

concentration for a higher wall charge since we extract electrolyte through the leaky wall surrounded by electrolyte of higher ionic concentration. For large electric potential differences, the concentration increases in the main channel (the advective contribution to the anion current density cancels the electric contribution) and decreases rapidly in the vortex. The vortex provides large mixing of the electrolyte, and the extend of the depletion region is determined by the size of this vortex, i.e. the width of the outlet channel. This effect is elucidated in figure 6.6 (a) where the normalized total ionic concentration is plotted as function of x in the channel for $\sigma = -1 \text{ mC/m}^2$, $p_0 = 0 \text{ Pa}$, $V_0 = 100V_T$, and different widths of the outlet channel W_{outlet} . In the figure, the position of the left boundary of the outlet channel is marked with a dashed line, and we clearly see the tendency that the large concentration gradient is centred around this boundary. The diffusive contribution to the current is responsible for smoothing out this rapid drop in concentration. As the width of the outlet channel increases, the vortex becomes less dominating (provides less mixing) and we see in figure 6.6 (b) a flow rather similar to the flow studied in figure 5.7 (b).

When a pressure difference is applied (figure 6.4 (b)), we see a small indication that charged walls might provide better desalination: For small V_0 , charged walls provide a lower outlet concentration for a given flow rate and the points at $V_0 = 7V_T$ show slightly lower concentration the higher the wall charge. The effect, however, is quite small and does not provide clear conclusions. However, it suggests that charged walls might provide extended depletion if the vortex can be suppressed by a pressure-driven flow. This supposition is examined in section 6.2.2. Note that the flow rate in figure 6.4 (b) for $V_0 = 0V_T$ decreases for higher wall charges. An increase in wall charge increases the cation concentration around the leaky wall. In front of the leaky wall, flow carries ions into the equilibrium Debye layer, and on the rear of the leaky wall, flow removes cations from the Debye layer. This tends to slow down the electrolyte.

The curves in figure 6.4 (a) have a plateau of almost constant outlet concentration for V_0 around $20V_T$ to $35V_T$. In this electric potential range, the outlet concentration is balanced

between a small lowering in concentration just in front of the membrane and an increase in concentration further from the membrane (see figure 6.5 (b.2,3)). However, since most of the electrolyte is flushed out from just in front of the membrane, the concentration decreases slightly. For even higher electric potentials, the curves flattens as the concentration tends towards a limiting profile at high flow rates (when the concentration gradient increases in front of the outlet channel, as in figure 6.6 (a) for $W_{\text{outlet}} = 0.5 \mu\text{m}$ at $V_0 = 100V_{\text{T}}$).

We note that for $\sigma = -3 \text{ mC/m}^2$, the velocity in the vortex is up to $3 \times 10^{-2} \text{ m/s}$ (for $V_0 = 70V_{\text{T}}$). Considering H as the characteristic dimension for the confinement of this vortex we have $\rho H/\eta = 1 \text{ s/m}$, thus $Re = 3 \times 10^{-2}$. Hence, we still do not expect the non-linear term in the Navier–Stokes equation to dominate. However, for larger velocities, we approach the regime where we should be careful about the assumption of neglecting the non-linear contribution.

We conclude, that the observation of worsened desalination for an increasing wall charge is due to a combination of the transverse concentration gradient, thus we extract electrolyte through the leaky wall containing electrolyte of high concentration, and the vortex formed in front of the outlet channel. In this model, we find that uncharged walls provide better desalination. However, we should not per se extend this conclusion to the macroscopic system. We found, as we increased the width of the outlet channel, that the contribution from the vortex was less pronounced for small electric potential differences. The extend of the depletion region due to overlimiting current scales linearly with the length of the channel (when advection is neglected), as discussed in chapter 5, whereas the vortex seems to dominate on a smaller length scale. However, the model does suggest some important points: The results indicate that the transverse concentration gradient does contribute to the concentration of extracted electrolyte. This is examined further in the next section by considering asymmetrically charged walls. Furthermore, since electro-osmotic flow carries electrolyte of high ionic concentration towards the depletion region, it suggests that it might benefit to impose a transverse pressure-driven flow. This would also suppress the longitudinal advective contribution and the formation of a vortex, thus allow charged walls to contribute to an extended depletion region. This is examined in section 6.2.2.

6.2 Modified systems

6.2.1 Asymmetric wall charge

In order to understand how the transverse concentration gradient affects the outlet concentration, we consider a channel with asymmetrically charged walls. We place an outlet channel in only one side of the main channel, and apply a surface charge on the opposite wall as illustrated in figure 6.7 (a). The specific numerical set-up is illustrated in the appendix figure A.1.

The relative outlet concentration is plotted in figure 6.8 (a) as function of flow rate $Q = \int_{\partial\Omega_s} dxv_y$ for the case of $p_0 = 0 \text{ Pa}$ and varying σ . Note that the flow rate for a given electric potential difference decreases compared to figure 6.4 (a) since we only have an outlet channel in one side of the main channel. However, in spite of a slightly lower flow rate, the behaviour of the systems for $\sigma = 0 \text{ C/m}^2$ looks similar, as we would expect.

By comparison of figure 6.4 (a) and figure 6.8 (a) we find a lower outlet concentration for a given flow rate (and a given electric potential difference) for the system with asymmetrically charged walls. For $\sigma = -3 \text{ mC/m}^2$ and a flow rate of $Q = 4 \times 10^{-9} \text{ m}^2 \text{ s}^{-1}$, the relative outlet concentration is decreased from 1.2×10^{-2} (symmetric wall charge) to 3.9×10^{-4} (asymmetric wall charge). This suggests that the transverse concentration gradient provides a considerable contribution to the outlet concentration. To neglect this contribution in a macroscopic model might be a crude approximation.

6.2.2 Transverse pressure-driven flow

In the system with symmetrically charged walls, we found that the vortex in front of the outlet channel determined the extend of the depletion region which explained why desalination worsened for a higher wall charge. We consider a system with a transverse flow channel as seen in figure 6.7 (b) [15]. For the numerical simulations, we set $H = L = 1 \text{ }\mu\text{m}$ and $H_{\text{inlet}} = H_{\text{outlet}} = 3 \text{ }\mu\text{m}$. The specific numerical set-up is illustrated in the appendix, figure A.2.

The outlet concentration as function of electric potential difference is plotted in figure 6.8 (b). Since electrolyte of high ionic concentration flows with high pressure into the system, we find a higher outlet concentration compared to the previous systems. However, one could imagine numerous of these channels connected, thus providing lower outlet concentration. The interesting observation is that we clearly find smaller outlet concentration the higher the wall charge for a given electric potential difference. The total ionic concentration (averaged over the height of the channel in front of the membrane and normalized to the concentration at

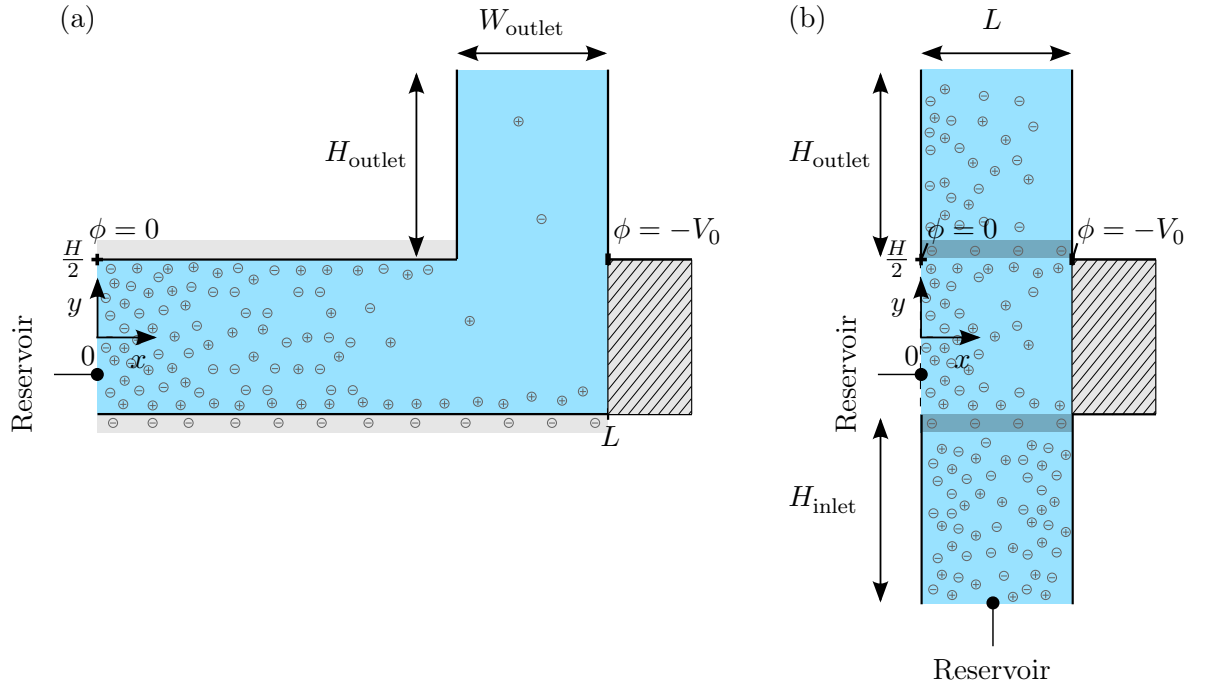


Figure 6.7: Modified systems: (a) Channel with asymmetrically charged walls. (b) Channel with a transverse pressure-driven flow.

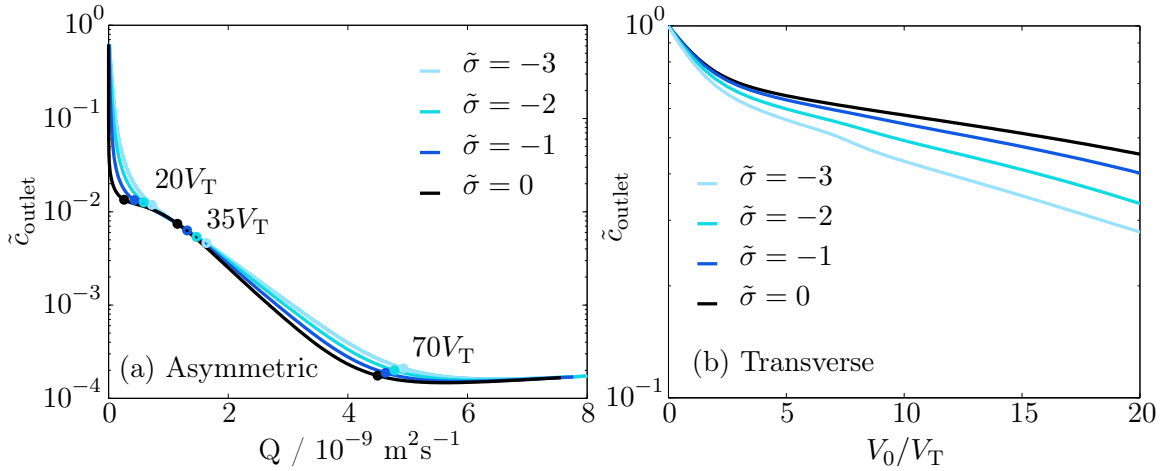


Figure 6.8: (a) Total ionic concentration of extracted electrolyte relative to the concentration at the inlet as function of flow rate for varying wall charge for the channel with asymmetrically charged walls. (b) Total ionic concentration of extracted electrolyte relative to the concentration at the inlet as function of electric potential difference for the channel with a transverse pressure-driven flow.

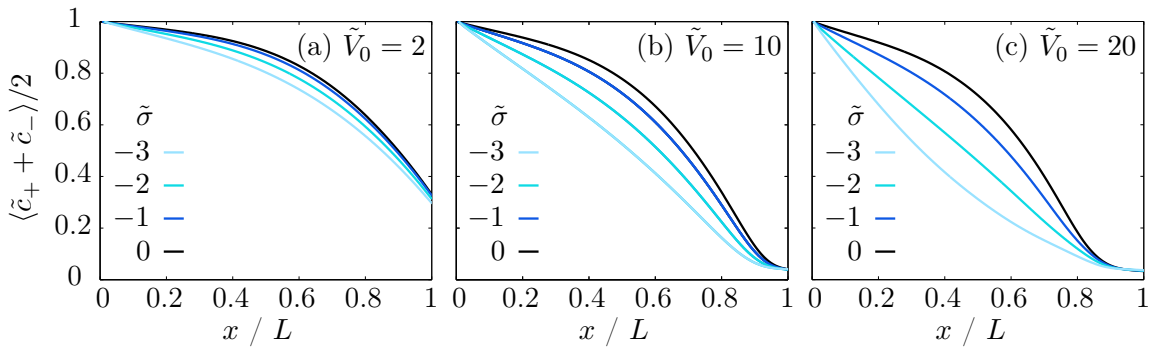


Figure 6.9: Concentration (averaged over the height of the channel in front of the membrane and normalized to the concentration at the left reservoir) as function of x for varying wall charges and an electric potential difference of $V_0 = 2V_T$ (a), $V_0 = 10V_T$ (b), and $V_0 = 20V_T$ (c) for the system with a transverse flow channel.

the left reservoir) is plotted in figure 6.9 as function of x for varying wall charges and varying electric potential differences. The vortex is suppressed by the large Poiseuille flow flushing transverse through the system, thus allowing charged walls to provide extended depletion and a lowering of the outlet concentration. In order to reduce the contribution from the electroosmotic flow and to suppress the formation of a vortex it would seem reasonable to impose such a transverse pressure-driven flow of seawater in a macroscopic desalination device.

7 | Conclusion and outlook

In this thesis we have studied electrokinetics in microchannels with ion-selective membranes. We explained the well-known phenomena of a Debye screening layer in an electrolyte near a charged surface, and presented an analytical and numerical model of a microchannel with a cation-selective membrane exhibiting concentration polarization in response to an electric field. Conduction in the Debye layers provided overlimiting current and extended depletion in the electrolyte. In the numerical study, we found that electro-osmotic flow carries electrolyte of high ionic concentration near charged walls, which provides a transverse concentration gradient in addition to the longitudinal concentration polarization.

In order to study applications for desalination and how electrokinetic effects contribute in a desalination device, we presented a numerical model of a microchannel with outlet channels implemented in front of the cation-selective membrane. This provides a simple model of the microchannels effectively formed in a glass frit in the desalination device studied by the group of Henrik Bruus at DTU and the group of Martin Bazant at MIT. In order to model the conductive path in the glass frit, we implemented a *leaky* wall in front of the outlet channel which maintains the same wall charge as the remaining wall but allows electrolyte to flow through.

We found that charged walls did not provide extended depletion in the system, which resulted in worsened desalination due to the higher ionic concentration near the charged walls and the leaky walls. The depletion region was governed by a vortex providing large mixing in front of the outlet channel. As we increased the width of the outlet channel, the contribution from the vortex was less pronounced. Since the extend of the depletion region due to overlimiting current scales linearly with the length of the channel (when advection is neglected), whereas the vortex seems to dominate on a smaller length scale, we should not per se extend this conclusion to the macroscopic system. However, the model indicates the important points that the transverse concentration gradient might provide a non-negligible contribution to the concentration of the extracted electrolyte in the macroscopic desalination device. By considering a channel with asymmetrically charged walls, we found much improved desalination. Furthermore, the results suggest that it might benefit to consider a system with a transverse pressure-driven flow which would minimize the contribution of electro-osmotic flow and suppress the formation of a vortex.

For further study, one could examine the system with a transverse flow channel even further. For instance, one could implement a rigid wall instead of the reservoir to the left of the membrane, and implement a partition wall in the outlet channel to divide extracted electrolyte of high and low concentration. It could also provide important information if one could establish a one-dimensional model of the channel including the transverse concentration gradient

Chapter 7. Conclusion and outlook

to acquire further knowledge of the contribution from the higher ionic concentration near charged walls. Furthermore, even though we can learn much by studying the microchannels formed in the glass frit, it is difficult to achieve quantitative results about the performance of a macroscopic device from this microscopic view. The next step would be to consider how to implement a macroscopic model of the system. A first step could be to include Darcy's law of a porous material into the Navier–Stokes equation, and from this, consider whether it is possible to include a way of describing the contribution from electro-osmotic flow.

For future work it is also crucial to combine theoretical considerations with knowledge from experiments. Together, this could provide further insight into this complex but exciting physical system.

A | Appendix

A.1 Asymmetric wall charge

At $\partial\Omega_1$ we apply the constraints

$$c_{\pm}(y) = c_0 \exp\left(\mp 4 \operatorname{arctanh}\left[\tanh\left(\frac{\zeta}{4V_T}\right) \exp\left(-\frac{y}{\lambda_D}\right)\right]\right), \quad (\text{A.1})$$

$$\phi(y) = 4V_T \operatorname{arctanh}\left[\tanh\left(\frac{\zeta}{4V_T}\right) \exp\left(-\frac{y}{\lambda_D}\right)\right]. \quad (\text{A.2})$$

At $\partial\Omega_4$ we apply the constraint

$$\phi(y) = 4V_T \operatorname{arctanh}\left[\tanh\left(\frac{\zeta}{4V_T}\right) \exp\left(-\frac{y}{\lambda_D^*}\right)\right] - V_0, \quad (\text{A.3})$$

where the concentration in λ_D is measured by a probe at the midpoint of $\partial\Omega_4$.

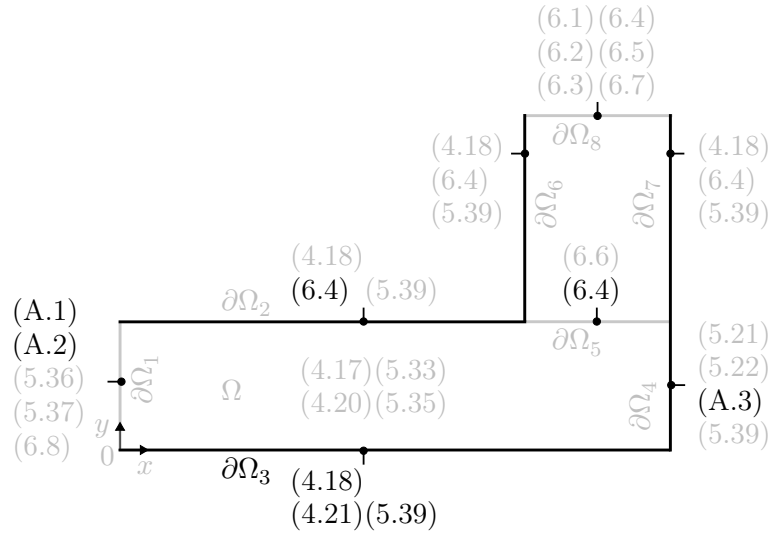


Figure A.1: Schematic illustration of the numerical set-up of the channel with asymmetrically charged walls. The rigid walls $\partial\Omega_2$, $\partial\Omega_3$, $\partial\Omega_6$, $\partial\Omega_7$, and membrane $\partial\Omega_4$ are drawn in black, and the inlet $\partial\Omega_1$, outlet $\partial\Omega_8$, and leaky wall $\partial\Omega_5$ are drawn in grey. Numbers in parenthesis refer to the equation number of the governing equation or boundary condition.

A.2 Transverse pressure-driven flow

At $\partial\Omega_1$, since $\lambda_D \ll H$, we apply the constraints

$$c_{\pm}(y) = c_0 \exp \left(\mp 4 \operatorname{arctanh} \left[\tanh \left(\frac{\zeta}{4V_T} \right) \exp \left(-\frac{y}{\lambda_D} \right) \right] \right),$$

$$+ c_0 \exp \left(\mp 4 \operatorname{arctanh} \left[\tanh \left(\frac{\zeta}{4V_T} \right) \exp \left(-\frac{(H-y)}{\lambda_D} \right) \right] \right), \quad (\text{A.4})$$

$$\phi(y) = 4V_T \operatorname{arctanh} \left[\tanh \left(\frac{\zeta}{4V_T} \right) \exp \left(-\frac{y}{\lambda_D} \right) \right]$$

$$+ 4V_T \operatorname{arctanh} \left[\tanh \left(\frac{\zeta}{4V_T} \right) \exp \left(-\frac{(H-y)}{\lambda_D} \right) \right]. \quad (\text{A.5})$$

At $\partial\Omega_4$ we apply the constraint

$$\phi(y) = 4V_T \operatorname{arctanh} \left[\tanh \left(\frac{\zeta}{4V_T} \right) \exp \left(-\frac{y}{\lambda_D^*} \right) \right]$$

$$+ 4V_T \operatorname{arctanh} \left[\tanh \left(\frac{\zeta}{4V_T} \right) \exp \left(-\frac{(H-y)}{\lambda_D^*} \right) \right], \quad (\text{A.6})$$

where the concentration in λ_D is measured by a probe at the midpoint of $\partial\Omega_4$.

At $\partial\Omega_{10}$ we apply the constraints

$$c_{\pm} = c_0, \quad (\text{A.7})$$

$$p = p_0. \quad (\text{A.8})$$

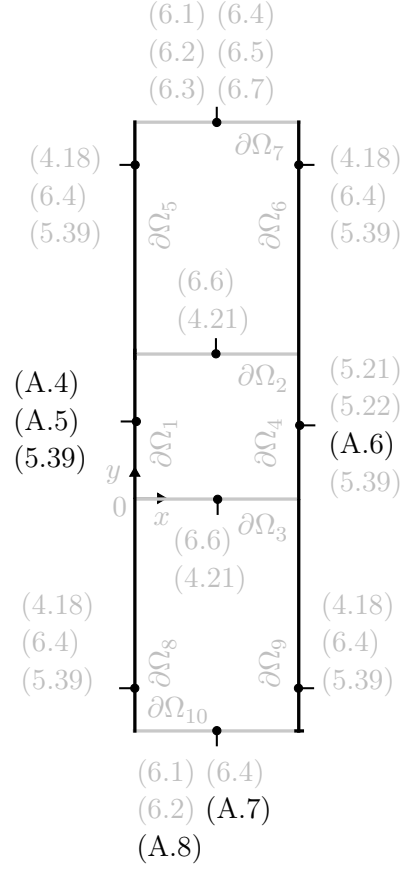


Figure A.2: Schematic illustration of the numerical set-up of a channel with a transverse pressure-driven flow. The rigid walls $\partial\Omega_5$, $\partial\Omega_6$, $\partial\Omega_8$, $\partial\Omega_9$, reservoir $\partial\Omega_1$, and membrane, $\partial\Omega_4$, are drawn in black, the inlet $\partial\Omega_{10}$, outlet $\partial\Omega_7$, and leaky walls $\partial\Omega_2$, $\partial\Omega_3$ are drawn in grey. Numbers in parenthesis refer to the equation number of the boundary condition. Governing equations are similar to figure A.1.

Chapter A. Appendix

Bibliography

- [1] M. Parry, O. Canziani, J. Palutikof, P. v. d. Linden, and C. Hanson, *Climate change 2007: Impacts, adaptation and vulnerability, working group II contribution to the Fourth Assessment Report of the IPCC* (Cambridge University Press) (2008).
- [2] H. Bruus, *Theoretical microfluidics*. No. 18 in Oxford master series in physics (Oxford University Press, Oxford) (2008).
- [3] H. Gould and J. Tobochnik, *Statistical and thermal physics : with computer applications* (Princeton University Press) (2010).
- [4] P. Tabeling, *Introduction to microfluidics* (Oxford University Press) (2005).
- [5] D. Griffiths and R. College, *Introduction to electrodynamics* (Prentice Hall) (1999).
- [6] C. P. Nielsen, *Introduction to weak form modeling in comsol* (2013).
- [7] F. Sayas, *A gentle introduction to the finite element method* (2008).
- [8] P. B. Muller, R. Barnkop, M. J. H. Jensen, and H. Bruus, *A numerical study of microparticle acoustophoresis driven by acoustic radiation forces and streaming-induced drag forces*. LAB ON a CHIP **12**(22), 118301 (2012).
- [9] E. V. Dydek, B. Zaltzman, I. Rubinstein, D. S. Deng, A. Mani, and M. Z. Bazant, *Overlimiting current in a microchannel*. Phys Rev Lett **107**(11), 118301 (2011).
- [10] C. P. Nielsen, *Theory and Simulation of Electrokinetics in Micro- and Nanochannels*. Master's thesis, Technical University of Denmark (2012).
- [11] S. Kershaw and A. Cundy, *Oceanography : an earth science perspective* (Stanley Thornes) (2000).
- [12] M. B. Andersen, M. van Soestbergen, A. Mani, H. Bruus, P. M. Biesheuvel, and M. Z. Bazant, *Current-induced membrane discharge*. Physical Review Letters **109**(10), 108301 (2012).
- [13] S. K. Hansen, E. P. Sensiuis, and M. G. Sensiuis , *Theory of electrohydrodynamic effects in microfluidics; desalination* (2013), physics project.
- [14] M. Z. Bazant, E. V. Dydek, D. Deng, and A. Mani, *Method and apparatus for desalination and purification*. Patent Application Publication (2011).

Bibliography

- [15] M. Z. Bazant and E. V. Dydek, *Nonlinear dynamics of ion concentration polarization in porous media: The leaky membrane model*. *AIChE Journal* **59**(9), 3539–3555 (2013).